



TECHNISCHE UNIVERSITÄT BERLIN

MASTERARBEIT

Simulation of Solid Angle Effects in the Detection of X-ray Fluorescence upon Investigation of Inhomogeneous Samples

Hanna Dierks

Erstgutachterin: Prof. Dr. Birgit KANNGIESSER

Zweitgutachter: Dr. Burkhard BECKHOFF

Betreuer: Dr. Lars LÜHL

Fakultät II - Mathematik und Naturwissenschaften
Institut für Optik und Atomare Physik
AG Analytische Röntgenphysik

29. März 2018

Eidesstattliche Erklärung

Hiermit erkläre ich, dass ich die vorliegende Arbeit selbstständig und eigenhändig sowie ohne unerlaubte fremde Hilfe und ausschließlich unter Verwendung der aufgeführten Quellen und Hilfsmittel angefertigt habe.

Die selbstständige und eigenhändige Anfertigung erkläre ich an Eides statt.

_____ Berlin, den _____
Unterschrift *Datum*

Contents

1 Soft/Tender X-Ray Microscopy	5
1.1 Scanning Transmission X-Ray Microscopy	6
1.2 Fluorescence Microscopy	7
1.3 Optics - Fresnel Zone Plates	7
1.4 Fluorescence Detection: Silicon Drift Detector	11
1.4.1 Electronic Noise	12
1.4.2 Detector and Scattering Artifacts	13
1.5 Spatial Resolution	14
1.5.1 Experimental determination of the spatial resolution .	17
1.6 State of the Art: soft/tender STXM with Fluorescence Mode .	18
1.7 Application: Biological Samples	19
2 X-Ray Fluorescence Theory	23
2.1 The Fundamental Parameter Approach - Sherman Equation .	24
2.1.1 Bulk Samples	26
2.1.2 Layered Samples	29
3 Motivation for a large Solid Angle Approach	31
3.1 Solid Angle	31
3.2 Incident and Observation Angle Variation: Literature Review	32
3.3 Inhomogeneous Samples	35
3.4 Implications of Large Solid Angles on Spatial Resolution .	36
3.5 Quantitative Imaging	37
4 Experimental Setup: AnImaX	39
4.1 The new QUAD Detector	40
5 Simulation Approach: QUADaps	45
5.1 The xrfLibrary	45
5.2 Model Assumptions	47
5.3 Simulated Sample Layout: Possibilities and Limits	47

5.4	The Coordinate System	48
5.5	Area Decomposition of the Detector	49
5.6	Beam Position along Z	51
5.7	2D Considerations	53
5.8	3D Considerations	59
6	Results	61
6.1	Stability Tests of the Algorithm and Error Estimation	61
6.2	Solid Angle and Working Distance	64
6.3	Simulation Results	66
6.3.1	Homogeneous Samples - Comparison to Equivalent Angles	68
6.3.2	Homogeneous Samples - Surface Structures	69
6.3.3	Inhomogeneous Samples - Information Depth	72
6.3.4	Inhomogeneous Samples - Area Mapping	78
6.4	Comparison to Experimental Results	81
7	Conclusion and Prospect	85

Deutsche Zusammenfassung

Röntgenmikroskopie im Energiebereich von 100 eV bis 5 keV ist ein wichtiges Verfahren um biomedizinische Proben auf zellulärer Ebene zu untersuchen. Rasterverfahren ermöglichen die gleichzeitige Messung von Transmissions- und Fluoreszenzsignal, sodass die Morphologie und die räumliche Verteilung der chemischen Elemente (Kohlenstoff bis Molybdän) mit einer räumlichen Auflösung von unter 100 nm abgebildet werden kann. Da biologische Proben im Allgemeinen nur ein schwaches Fluoreszenzsignal emittieren, wird für kurze Messzeiten eine hohe Detektoreffizienz benötigt. Das AnImaX Röntgenmikroskop ist daher mit einem neuen QUAD SDD (*Bruker Nano*) ausgestattet, welcher einen sehr großen Raumwinkel abdeckt (bis zu 1.1 sr) und somit Messzeiten von unter 100 ms pro Punkt ermöglicht.

Herkömmliche Quantifizierungsansätze für Röntgenfluoreszenz sind nur für kleine Detektionsraumwinkel gültig. Für den QUAD Detektor sind neue Effekte zu erwarten, da die gemessene Strahlung in einem großen Bereich an verschiedenen Austrittswinkeln detektiert wird. Daraus folgen geometrisch unterschiedliche Absorptionsweglängen in der Probe und, für inhomogene Proben, verschiedene chemische Zusammensetzungen bzw. Absorptionskoeffizienten. In der vorliegenden Arbeit werden diese Effekte basierend auf der Sherman Gleichung und einer virtuellen Zerlegung des QUAD Detektors simuliert und mit ersten Experimenten am Synchrotron belegt. Die mit dem Simualtionsprogramm möglichen Vorwärtsrechnungen dienen als erster Schritt hin zu neuen Quantifizierungsansätzen für Röntgenfluoreszenzmessenungen unter großen Raumwinkeln.

Abstract

Soft and tender X-ray microscopy (XRM) at cellular level is used worldwide to investigate biomedical samples. Scanning transmission X-ray microscopy (STXM) in combination with fluorescence detection is able to map elements from C to Mo with a lateral resolution below 100 nm. Since biological samples generally emit rather weak fluorescence signals, a high detector efficiency (e.g. large solid angle) is necessary to avoid long measurement times. The AnImaX end station is equipped with a new annular QUAD detector which yields a very large solid angle of detection (up to 1.1 sr). Established quantification approaches normally assume a small detector area with respect to the distance sample to detector, limiting the solid angle. For large solid angles, new effects occur, since the detected radiation passes a wide angular range on its way out of the sample. This results in geometrically different exit path lengths and, for inhomogeneous samples, even different sample composition (resp. absorption coefficients). In the following thesis, these effects are simulated based on the Sherman equation combined with an additional virtual decomposition of the sample and detector. Moreover, first experiments at the synchrotron confirm the predicted effects. The now possible forward calculations aim to be a first step towards the development of new quantification concepts for annular detectors with a large solid angle.

Introduction

X-Ray microscopy in the soft and tender energy regime is becoming an increasingly important tool for studying various samples from the life sciences at a resolution in the range of several tens of nanometers. The combination of scanning transmission (STXM) and fluorescence mode, as implemented at the new flexible AnImaX end station for P04 at Petra III (DESY Hamburg) offers a range of complementary information about the sample. Available imaging options include absorption and phase contrast imaging in transmission as well as the lateral elemental distribution from the fluorescence signal.

Since biological samples generally emit weak fluorescence signals, a high detector efficiency (e.g. large solid angle) is necessary to avoid long measurement times. The AnImaX end station is equipped with a new annular QUAD detector (*Bruker Nano*) which yields a very large solid angle of detection (up to 1.1 sr).

The detector is composed of 4 independent SDD cells in a circular arrangement resembling a cloverleaf. The incident beam passes through a hole in the center of the detector, hitting the sample perpendicular to the surface. Established quantification approaches for X-ray fluorescence (such as the fundamental parameter approach using the Sherman equation) normally assume a small detector area with respect to the distance sample to detector, limiting the solid angle and making a narrow beam assumption possible. For large solid angles new effects occur, since the detector collects the radiation over a wide range of exit angles. This results in geometrically different exit path lengths and, for inhomogeneous samples, different absorption coefficient in each direction. The fluorescence signal thus shows artifacts due to the varying absorption. Since microscopy applications traditionally are supposed to show inhomogeneities, it is important to identify and distinguish these effects in comparison to features inherent to the sample.

The 4-element design of the QUAD detector makes this effect observable:

each cell measures the fluorescence signal from a different direction. Absorption of the primary fluorescence caused by inhomogeneities in the sample and/or surface structures attenuates the signal differently for each exit path. The signal thereby contains additional information, which might be usable for new quantification approaches.

In the following, these effects are simulated based on the Sherman equation as implemented in the *xrfLibrary* package for Python combined with an additional virtual decomposition of the sample and detector.

Depending on the simulated sample and experimental conditions (excitation energy, intensity, distances etc.) line scans and area maps can be generated showing inhomogeneity effects caused by surface structures, varying sample composition or density. The absorption mainly shows in shadow and enhancement effects at zone borders, comparable to known artifacts in scanning electron microscopy. The developed simulation program QUADaps is thus used to study these effects for various sample designs.

Additionally, the effect on fluorescence intensities for homogeneous samples is studied and existing correction approaches (such as equivalent angles) are reviewed.

Moreover, the first verification measurements were performed at the synchrotron BESSY II, experimentally confirming the predicted shadow effects.

Chapter 1

Soft/Tender X-Ray Microscopy

X-ray microscopy is considered to fill the gap between Scanning Electron Microscopy (SEM) and microscopy with visual light. Following the Abbe resolution limit (see Section 1.5) for full field microscopy, the resolution d is dependent on the wavelength λ and the numerical aperture NA_{obj} of the objective:

$$d = \frac{\lambda}{2n \cdot \sin(\alpha)} = \frac{\lambda}{2\text{NA}_{obj}} \quad (1.1)$$

Assuming a perfect objective with an $\text{NA} = 1$ neighboring objects with a distance down to half of the wavelength of the illuminating light can be distinguished. The smaller wavelength of X-rays compared to visual light leads to a possible higher spatial resolution of X-ray microscopy.

Due to the even smaller wavelength of electrons an even higher resolution can be achieved in electron microscopy (EM). But since electrons generally have a much shorter interaction path length in matter than photons, all EM techniques are mainly surface sensitive and/or demand very thinly sliced samples. Due to the charge transfer electrons cause, furthermore only a limited range of conductive samples are measurable and/or a sophisticated sample preparation is necessary. EM techniques can thus generally not be considered non-intrusive or non-damaging, which can be an important requirement especially when dealing with samples from biology or archeometry.

The soft to tender X-ray regime is commonly defined as ranging from 100 eV – 5 keV (10 nm – 0.5 nm) and includes the so called “water window” (280 - 530 eV, 2.34-4.4 nm).

The water window is defined by the absorption edges of carbon (as found mainly in living cells) and oxygen (mainly in water). The absorption contrast in biological samples thus makes it e.g. possible to distinguish between cells and inter cellular matter, if the incident light has an energy in the water

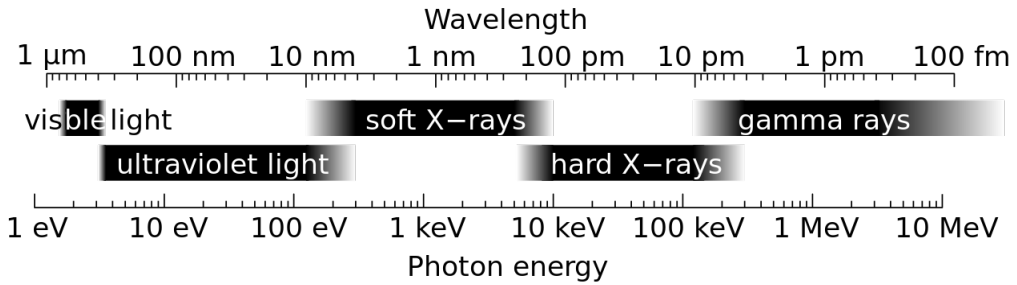


Figure 1.1: Common distinction of X-ray energy/wavelength ranges (from [18]).

window.

1.1 Scanning Transmission X-Ray Microscopy

Optical transmission microscopes are often realized in full-field setups, which include at least one magnifying lens (the objective). The magnification is dependent on the distances and lens properties and can be greatly enhanced when using several lenses. As the name suggests, the full field of view is imaged at once.

Since optical elements for X-rays are generally complicated to manufacture and have only a rather limited efficiency, it is favorable to have a setup with as few optical elements as possible.

The scanning transmission X-ray microscopy (STXM) uses a different approach. The image generation is realized by focusing the incident beam on a small spot on the sample and scanning the sample area. At each scan point the transmission through the sample is detected and the resulting intensity values for each scan point are combined to a image by the computer.

The resolution of such a scanning microscope is dependent on the chosen step width for the scan and the size of the focal spot on the sample. The diffraction limit as described by the Abbe criterion is a fundamental lower limit. For synchrotron setups it is common to move the sample stage instead of the incident X-ray beam.

Since the intensity transmission of the sample is detected, the resulting image shows mainly the absorption contrast for the illuminating energy. Phase contrast is not directly accessible, but there are recent approaches to include e.g. Ptychography into STXM setups, which make phase retrieval possible. In case an area detector (e.g. a CCD) is used to measure the transmission, it is moreover possible to apply further data manipulation. Instead of only

considering the integrated intensity for each scan point, it is e.g. possible to calculate the dark field and differential phase contrast from the single images detected for each scan point.

Moreover additional, non-transmission signals, like the fluorescence signal or photo electrons, can be detected simultaneously, because of the possibility to directly correlate the small excited spot on the sample to the signal. This makes scanning microscopy a highly flexible method.

Nevertheless, it has to be noted that in contrast to full-field microscopy scanning microscopy needs much longer measurement times and the achieved resolution is often additionally limited by experimental parameters.

1.2 Fluorescence Microscopy

X-ray fluorescence as described in Section 2 makes (quantitative) elemental sample analysis possible. As noted above, it is possible to combine fluorescence detection with transmission detection in a scanning setup. The correlation of elemental composition and morphology yields important information to answer various bio-chemical research questions.

At each scan point a full X-ray fluorescence spectrum is recorded. The characteristic fluorescence lines in the spectra can thus be used to associate each scan point with a certain elemental composition.

There are different approaches to evaluate fluorescence spectra and visualize the fluorescence intensities (quantitative imaging: concentrations) of the contained elements.

For a rough and fast overview it is often sufficient to set regions of interest (ROI, here energy intervals) containing the characteristic lines of the respective elements and summing the fluorescence intensity (counts) in these ROIs. A more exact spectrum evaluation requires a deconvolution of the characteristic lines, background stripping, the consideration of detector effects (escape peaks, pile-up, sensitivity etc.). A careful fit of the spectra and a reference sample based backwards calculation using the fundamental parameter (FP) approach described in Section 2.1 combined with well-known experimental conditions can in principle make semi-quantitative imaging possible (see 3.5).

1.3 Optics - Fresnel Zone Plates

As stated above microscopy uses optical elements to generate a real space intensity pattern, the image. As the real part of the refractive index $n = 1 - \delta + i\beta$ for soft X-rays is smaller and very close to 1 for most materials, they

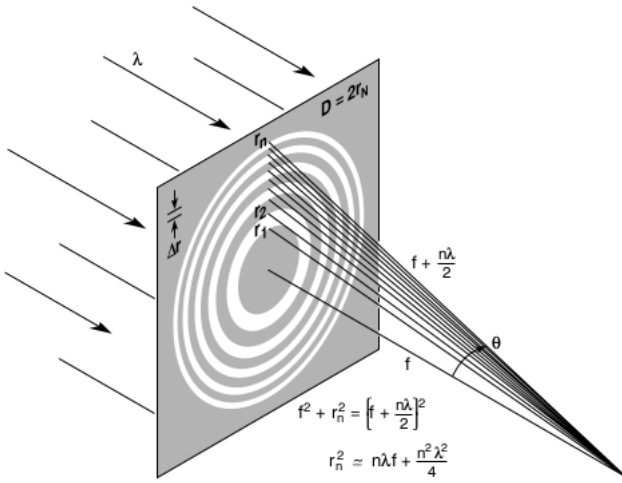


Figure 1.2: Illustration of a Fresnel zone plate and the corresponding distances and formulas. The angle θ is called α in the following text. (from [3]).

are not suited for building conventional optical elements like lenses and mirrors, which are based on refraction. The focusing necessary for microscopy is therefore not a trivial task in the (soft) X-ray regime. Several different optical elements like e.g. multilayer mirrors, Kirkpatrick-Beatz-Optics, polycapillary lenses and Fresnel zone plates have been developed to overcome this challenge.

The most commonly used focusing optics in soft X-ray microscopy are Fresnel zone plates. Due to their relatively high efficiency and flexibility, they were also chosen for the AnImaX project and shall be described here in more detail.

The focusing which can be achieved by Fresnel zone plates is based on diffraction occurring on sharp edges and the interference of the redirected waves. A conventional transmission Fresnel zone plate lens is a pattern of (flat) transparent and non-transparent rings and can be understood as a circular grid with varying line-width and spacing (see Figure 1.2). The rings are designed in a way that the path lengths difference between light passing through neighboring zones is one wavelength each and enables constructive interference. This is possible even with partially coherent radiation, although the best focusing is achieved with a high degree of spatial coherence.

Moreover all diffracted beams from each radial zone r_n need to cross at a focal spot in the distance f from the zone plate. This gives the Pythagorean

equation

$$r_n^2 + f^2 = \left(f + \frac{n\lambda}{2}\right)^2 \quad (1.2)$$

$$r_n^2 = n\lambda f + \left(\frac{n\lambda}{2}\right)^2 \quad (1.3)$$

which needs to be fulfilled (see Figure 1.2). Note that this equation is only valid for plane wave illumination ($\beta = 0$).

In the quadratic approximation it is assumed that the focal length is large compared to the wavelength $f \gg \frac{n\lambda}{2}$, this equals a small numeric aperture $\text{NA} = \sin(\alpha)$ (opening angle of the lens). Using this approximation, the radii r_n of the zones becomes

$$r_n = \sqrt{n\lambda f} \quad (1.4)$$

and the zone width of zone n can be described as the derivative of r_n (with $dn = 1$) :

$$dr_n = \frac{\lambda f}{2\sqrt{n\lambda f}} = \frac{\lambda f}{2r_n} = \frac{r_1}{2\sqrt{n}} \quad (1.5)$$

As the radii are dependent on the wavelength λ , a zone plate is designed for a specific energy and focal distance f . If it is used to focus light of a different energy, the focus will occur in a different focal plane

$$f = \frac{2r_N dr_N}{\lambda} \quad (1.6)$$

where the index N refers to the outermost zone. Similar to the description of equally spaced grating, several diffraction orders m occur at every zone edge. Analog to the derivation above ($m = 1$) one gets a focal spot for each diffraction order:

$$f_m = \frac{f}{m} \quad (1.7)$$

This means higher order foci are located closer to the zone plate.

The numerical aperture of a Fresnel zone plate is

$$\text{NA} = n_{material} \sin(\alpha) \approx 1 \cdot \tan \alpha = \frac{r_n}{f} = \frac{m\lambda}{2dr_n} \quad (1.8)$$

where m describes the diffraction order. The Rayleigh resolution criterion (discriminability of two neighboring point light sources with a lens with the numerical aperture NA, see Section 1.5) is

$$d = 1.22 \cdot \frac{\lambda}{2\text{NA}} = 1.22 \frac{dr_n}{m} \quad (1.9)$$

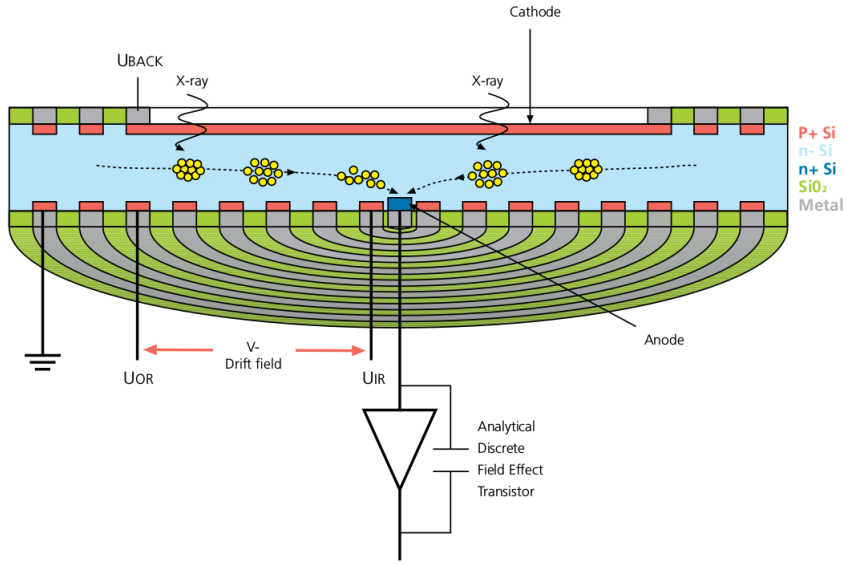


Figure 1.3: Illustration of the layout and operation a SDD (from [11]).

It becomes apparent, that this is equal to the outermost zone width except for the factor 1.22.

Moreover the resolution of a Fresnel zone plate is independent of the used wavelength, although the actual focal distance is not. Instead it is dependent on the outermost zone width dr_N , which is limited by manufacturing techniques.

Often the first diffraction order $m = 1$ is used for microscopy applications. The 0th diffraction order is passing the zone plate without being focused. Higher diffraction orders have a different focal plane (closer to the zone plate). All orders except the first need to be blocked before reaching the sample, to avoid an enlarged spot. This is done by a central stop on the zone plate and an additional pinhole of a slightly smaller diameter in the beam path, called the order sorting aperture (OSA).

Higher orders of diffraction $m > 1$ can yield a better focus, but carry less intensity. Negative diffraction orders result in a defocused cones (the virtual focal spot is on the other side of the lens) and are also blocked by the OSA.

1.4 Fluorescence Detection: Silicon Drift Detector

The increasing need for high energy resolution measurements for X-ray spectroscopy combined with short processing times at high count rates as necessary for mapping/imaging applications led to the development of energy dispersive Silicon Drift Detectors (SDD) as a replacement of traditional Si(Li) detectors.

Nowadays SDDs superseded Si(Li) detectors almost completely due to their better performance especially in the detection of low energy X-rays. They can be produced with a larger detector area and work at relatively high temperatures ($\approx -20^{\circ}\text{C}$), which makes cooling by an integrated Peltier element possible (in contrast to the more costly cooling with liquid nitrogen).

The active area of a conventional SDD is composed of a fully depleted, high-resistivity silicon crystal, a small-area collection anode (n^{+} Si) and a front contact area (p^{+} Si). Due to the small area of the collection anode, an additional electric drift field gradient is necessary to ensure the collection of the full charge cloud. This is realized by concentric ring electrodes on the backside of the chip. Commonly the Field Effect Transistor (FET) used in the pre-amplifier is directly integrated into the chip close to the anode. A schematic layout of a typical SDD chip is illustrated in Figure 1.3.

SDDs make energy dispersive detection of incoming X-rays possible. The detection principle is based on absorption of the photons by the silicon crystal and the following generation of electron-hole pairs. No wavelength dispersive element is therefore necessary.

The measurement process can be understood in a 4-step-model:

1. Absorption of the incoming photon and ionization of Si atoms. A charge cloud proportional to the energy of the photon is generated.
2. Drift of the electrons towards the collection anode, mediated by a electric field gradient applied by the ring electrodes.
3. Conversion of the charge to a voltage step at the FET pre-amplifier. The hight of the step is proportional to the original photon energy.
4. Measurement of the voltage step by the pulse processor and multi channel analyzer. The used shaping time directly influences the energy resolution.

In each of the above steps, certain effects can occur which influence the energy resolution of the measured signal, cause signal artifacts and contribute to the Signal to Noise Ratio (SNR).

1.4.1 Electronic Noise

Electronic noise is due to the detector parameters and readout settings. It mainly affects the energy resolution of the signal and the SNR. SDDs are generally considered to have a low electronic noise compared to Si(Li) detectors due to their different layout. A common analysis distinguishes 3 contributions to electronic noise:

$$N_{el} = N_V + N_{shot} + N_{1/f}$$

Voltage Noise N_V is mainly dependent on the sum of capacities C of the sensor and the FET gain.

$$\text{voltage noise} \approx \frac{kT}{g} \frac{C^2}{\tau_{shape}} \quad (1.10)$$

The largest contribution is the capacity of the anode which is itself proportional to the anode area. Since SDDs are characterized by a very small anode compared to their active area, the capacity is significantly lower than e.g. in Si(Li) detectors with a large area anode.

The noise can also be reduced by longer shaping times in the pulse processor. As a trade-off the smaller capacity allows for shorter shaping times which results in better energy resolution at high count rates.

Moreover a reduction of the temperature will decrease the thermal contribution to the noise.

Shot Noise N_{shot} is due to the leakage current between the electrodes. It is increased by the bias voltage applied to the active area, which generates the drift gradient. The leakage current gives rise to the underlying slope of the voltage ramp in the preamplifier output on which the photon events superimpose as sharp voltage steps. Therefore it can affect the energy resolution at long process times - the short process times possible with SDDs thus reduce this effect.

For a otherwise fixed detector layout, the leakage current is proportional to the area, thickness and operation temperature. Since the leakage current is reduced by the short process times of SDDs, they can be used at higher temperatures.

$\frac{1}{f}$ Noise $N_{1/f}$ is mainly independent of the shaping time, but proportional to the square overall capacity of the sensor, similar to the voltage noise.

1.4.2 Detector and Scattering Artifacts

Additional to the electronic noise which is mainly created in step 3 and 4 of the measurement process, several physical effects can occur in the sample (e.g. scattering) or in the ionization and drift process in the SDD, which create artifacts in the X-ray spectrum. These artifacts, if not recognized as such or corrected for, can lead to serious misinterpretation of the measured spectrum. Some of the artifacts are therefore often automatically corrected for in the measurement software. Nevertheless, it is worthwhile to consider their origin and effect, to identify them reliably.

The Pile Up Effect occurs when several X-ray photons reach the detector during the defined shaping time. The charge cloud generated by the respective photons thus reaches the anode in a time interval indistinguishable for the read-out electronics and are registered as belonging to only one photon event. The resulting height of the voltage step (resp. the measured energy) in this case is the sum of the single photon energies. This situation is only likely at a high count rate or very long integration times. Therefore SDD software often comes with the option to adjust the shaping time to the expected count rate.

Typically the SDD has two read-out channels to identify pile up directly. The fast channel has a very short shaping time and thus a bad energy resolution, the slow channel, which is actually used for the spectrum generation, has a longer shaping time. If only one voltage step is registered in the slow channel but several in the fast channel, this event is automatically ignored for the actual signal and instead added to the dead time. Nevertheless, if the events arrive too quickly for the fast channel, pile-up still can still occur in the spectrum. Pile up peaks always appear at sums or multiples of energies of intense X-ray lines (of the same as well as different elements), which helps to identify them.

Incomplete Charge Collection refers to the loss of electron-hole pairs, before they reach the read-out electrodes. This effect results in a low energy side tailing of the respective peak and is especially visible at low energy X-ray lines. Since low energy photons generally have a shorter penetration depth in the sensor, they generate charge clouds close to the surface. Parts of these clouds therefore often either recombine or parts of the energy is deposited in

the entrance window/electrodes. The same is true for flat incident angles. Low energy X-ray peaks are therefore often broader and their mean energy is shifted to a smaller value.

Escape Peaks are one of the possible effects of an incomplete charge collection. In this special case, a part of the absorbed energy causes the emission of a Si-K α fluorescence photon, normally close to the chip surface, which escapes the detector chip. The measured energy is therefore lower than the original energy of the incoming X-ray photon by $E_{Si} = 1.740\text{ keV}$. In the spectrum additional peaks at $E - E_{Si}$ are visible. They are normally much smaller than the actual peak and their counts need to be added to the peak at E to allow for a correct evaluation of the sample composition.

Bragg peaks are associated with the crystal structure of solid samples. They are dependent on the incident and observation angle and the orientation of the lattice in the sample as described by Bragg's diffraction law. They are normally easily distinguishable from sharp fluorescence lines by their broader shape and occur at high X-ray energies. They are very uncommon in biological samples.

Beside these artifacts, elastic (Rayleigh) and inelastic (Compton) scattering can lead to the loss or misinterpretation of counts. Moreover the named effects can happen in various combinations, depending on the experimental situation. The higher the order of the effect, the less prominent the artifacts in the measurement.

1.5 Spatial Resolution

One of the key parameters of a microscope (or any other imaging setup) is the spatial resolution which can be reached. Although the technological development aims at a constant improvement of the resolution, there is not yet an universal definition of spatial resolution which is consistent for all imaging techniques and scientific communities. A comparison of resolution values therefore always needs a thoughtful evaluation of the specific situation and might lead to confusion.

Even historically there are two main theoretical approaches used to define the resolution limit of an (optical) microscope: the Abbe and Rayleigh criterion.

Starting there a short overview of the most common definition of spatial resolution shall be given here. For the sake of simplicity, the mathematical

derivation of the respective criteria shall not be presented in detail. Nevertheless it is interesting to reconsider the experimental situation and principle assumptions that led to the formulas.

Ernst Abbe based his derivation on the Fourier theory of image formation, although he never explicitly used the term in his publication from 1873 [1]. Using the Fourier transformation, as a mathematical operation, Abbe concluded that an optical image is the Fourier transform of the Fourier transform of the object function.

The Fourier transformation in the spatial dimensions can be understood by the analogy of spacial frequencies and temporal frequencies. As any function or signal can be decomposed into an infinite sum of sine and cosines functions, every object can be imagined as consisting of an overlay of periodic grids with certain spacial frequencies (or periods). Each of these grids causes the diffraction of parts of the incoming light, the interference of all these diffractions is the signal coming from the specimen.

The light is thus diffracted by the object (1. Fourier transformation) and the imaging lens works as an inverse Fourier transformation, recovering the object function. Note that the optical elements themselves introduce a filter function, which alters the Fourier transform so that the inverse Fourier transformation ultimately reconstructs a convolution of object and filter function. This filter function is the so called point spread function.

Based on this idea, Abbe formulated the following restriction for a successful image formation:

“The structure of an object is resolved if at least the first diffraction order is propagated through the optical imaging system.” [1]

The ‘structure’ he refers to, can be understood as a lattice with lattice distance d , which diffracts the incoming light in certain angles θ , with the diffraction order m :

$$d \cdot n \sin(\theta) = \pm m\lambda \quad (1.11)$$

The numerical aperture NA of the lens limits the range of angles under which the light reaches the lens. Therefore the smallest structure which can be resolved is limited by:

$$d = 0.5 \cdot \frac{\lambda}{NA} \quad (1.12)$$

Note that for this criterion a tilted illumination is assumed under which the first diffraction order $m = 1$ is parallel to the optical axis of the lens (this introduces the factor $\frac{1}{2}$).

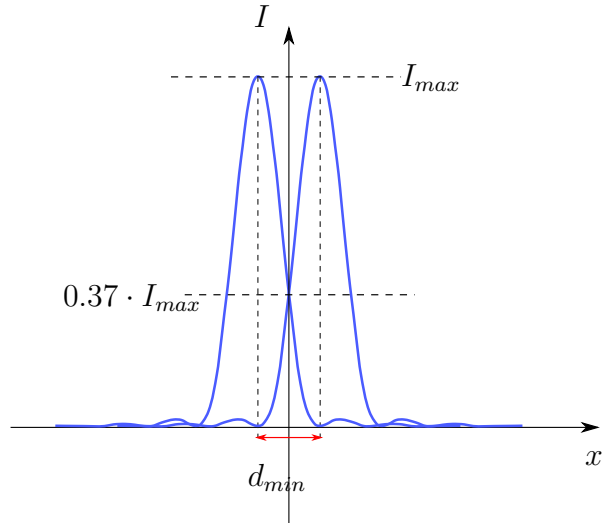


Figure 1.4: Minimal distance d_{min} of two point sources that still allows to distinguish between the sources. The point sources generate a Airy intensity pattern in the detection plane.

Rayleigh chose a different approach inspired by astronomical observations. Therefore his considerations are strictly speaking only valid for active light sources, not reflecting or transmitting samples. His criterion breaks down the idea, that “two point sources are still resolved if the center of the first Airy pattern is aligned with the first minimum of the second Airy pattern”. The Airy pattern is the intensity pattern of a point source imaged with an aberration free lens. It can be described by a Bessel function of the first kind. The application of the above restriction leads to a minimal distance between two point sources of

$$d_{min} = 0.61 \frac{\lambda}{NA} \quad (1.13)$$

Note that at this limit, in order to be still distinguishable in the image, the detected intensity distributions of the two (equally bright) sources intersect at about 37 % of their peak intensity (see Figure 1.4). Summing the intensity distributions, the overall intensity at the dip between the two maxima is $2 \cdot 37\% = 74\%$ of the peak intensities. Or, phrasing it differently, a minimum intensity dip of 26 % of the neighboring peak intensities is necessary to distinguish the two peaks.

Although both theoretical limits are derived starting from very different assumptions, they both result in quite similar formulas. Depending on the ex-

perimental situation, it needs to be decided which criterion should be used. Please note, that none of the named approaches is originally formulated for scanning microscopy or other computer based techniques, like coherent diffraction imaging (CDI) or ptychography.

1.5.1 Experimental determination of the spatial resolution

Although the theoretical limits described above are important for the planning of a microscope, they normally are not reached in the application. Therefore there are several experimental approaches to measure spatial resolution. Since they may lead to different results, it is necessary to pay close attention to which approach was used before comparing resolution values with each other.

Fastest and most common is the measurement of the intensity contrast at an edge. Assuming a sharp edge in the sample, the signal will show the convolution of the transfer function of the microscope and the step in the object function. The height and steepness of the recorded intensity step thus can be used as a measure for the resolution.

The spatial distance Δr in which the signal rises from 10 % to 90 % of the step height gives an idea about the achieved resolution. Alternatively the same criterion with thresholds at 25 % and 75 % can be used. Obviously the used thresholds values will lead to different resolutions for the same measurement. Generally, a smaller Δr means a better resolution.

Instead of only using the values at these intensity thresholds, it is possible to calculate the derivative of the whole intensity step. The resulting Gauss function is the line spread function of the microscope. Often the FWHM of this derivative is used as a measure for the resolution. This approach is meant to refer to the Rayleigh criterion, although Rayleigh originally used a 37 % threshold instead of a 50 % (= FWHM). This results in an overestimation of the resolution and can be corrected for by applying a additional factor on the FWHM value.

A more sophisticated approach is the measurement of the whole contrast transfer function e.g. by imaging a Siemens star. A Siemens star is a circular pattern of radial wedges. A cross Section along one radius will show a sequence of alternating intensity steps. The structure period thereby increases linearly with the radius. Thus, a wide range of spatial frequencies is directly

accessible with only one Siemens star.

The contrast transfer C is calculated as the relative intensity contrast

$$C = \frac{I_{max} - I_{min}}{I_{max} + I_{min}} \quad (1.14)$$

Calculating and plotting the contrast transfer as a function of the spatial frequency yields the contrast transfer function onto which the Rayleigh criterion can be applied: the smallest resolvable structure size is the inverse of the spatial frequency where the contrast transfer function falls under a certain threshold, usually 0.1.

This method gives a far more complete impression about the imaging properties of the used instrument, than a simple edge scan. As a drawback, it is necessary to have a suitable test object with high contrast and sharp features at hand, which might pose a problem for fluorescence in the soft x-ray regime. Moreover the measured contrast transfer function is only valid for the settings used to generate the Siemens star image. Changes of the setup e.g. refocusing on the actual sample, can change the resolution. Since it is often not possible to integrate this test pattern into the real sample, a edge scan at an accessible edge in the sample (plane) sometimes gives a more realistic impression of the achieved resolution in each measurement.

Since the resolution in scanning microscopy is highly dependent on the focus size on the sample, it needs to be mentioned here, that the resolution is also dependent on the thickness of the measured sample. For thick samples, the focus, describable as a Gauss beam focus, is not only limited by its waist size, but also by its focal depth. To achieve high resolution it is therefore important to chose the sample thickness according to the focal depth.

1.6 State of the Art: soft/tender STXM with Fluorescence Mode

Scanning X-ray microscopy with a fluorescence detection option in the soft to tender energy regime is still a rather young method and only a few setups exist worldwide. On the one hand this is due to the necessity of a source with a high brilliance and flux, which up to now makes it a sole synchrotron technique, on the other hand detectors with sufficient sensitivity that allow for short measurement times and a high signal-to-noise ratio are available only recently.

In the following a few examples which are comparable in layout, energy range and spatial resolution to the AnImaX setup shall be introduced. Since the field is constantly growing the information given are only valid for the current

state of the art.

The TwinMic end station at Elettra (Trieste, Italy) is equipped with a STXM with full-field option, as well as an array fluorescence detector close to the sample. Besides transmission imaging, near-absorption spectroscopy and fluorescence imaging is possible. The beamline has a energy range of 400-2200 eV, covering parts of the water window.

The current fluorescence detection system consists of 8 individual SDDs with an energy resolution of <135 eV FWHM at Mn K_α and a efficiency >90 % over the entire energy range. Each detector has a direct read-out channel and the solid angle is limited by the spatial compactness of the setup.

A planned update strives to replace the 8 single SDDs with a array of 4 monolithic, trapezoidal-shaped, multi-element detector tiles, each consisting of six hexagonal SDDs, arranged as a truncated pyramid [10]. The total active area is stated to be 728 mm², which covers about 11 % of the photoemission solid angle (\approx 1.38 sr). The average energy resolution of the new detector was measured as 150 eV FWHM at Mn K_α using a ⁵⁵Fe radioactive source.

The I08 beamline at the Diamond Light Source (Oxfordshire, England) is also dedicated to soft and tender X-ray microscopy. The energy range is with 250-4400 eV relatively broad. It offers STXM, NEXAFS/XANES, differential phase contrast, dark field and fluorescence imaging. The fluorescence detection is done by a conventional SDD, positioned at an angle to the sample surface.

A couple of other synchrotrons around the world also host STXM setups at soft/tender energy beamlines (without fluorescence detection) and more setups are planned or under development. In this context e.g. the Soft X-ray SpectroMicroscopy Facility 10ID-1 at the CLS (Saskatoon, Canada), NanoXAS- X07DB at SLS (Switzerland) and the BL08U beamline at SSRF (Shanghai, China) can be named.

1.7 Application: Biological Samples

Imaging is an important tool for biological and bio-medical research. Optical light microscopy is therefore a well established tool in almost every biology lab all over the world. Since the spatial resolution of visible light microscopy is traditionally limited by the used wavelength to a minimum of about 200 nm (not taking new super resolution microscopes into account), methods with

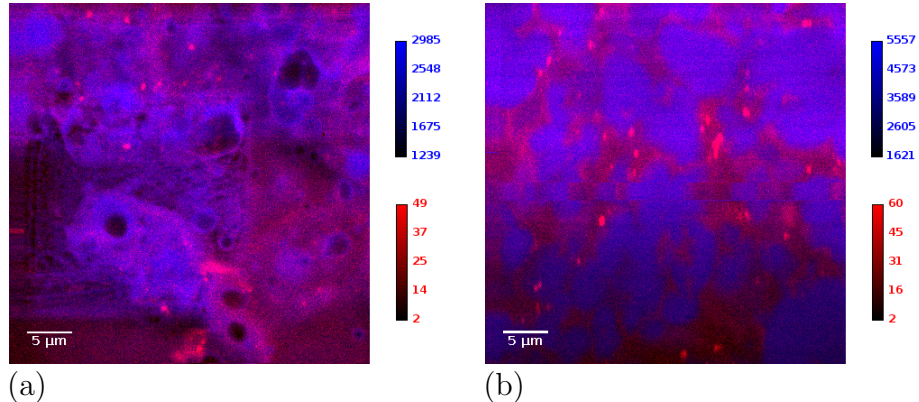


Figure 1.5: Iron (red) and carbon (blue) map of tissue slices of mice injected with SPIO marked lipoproteins. (a) mouse kept at 4 °C for 24 h, (b) mouse kept at 24 °C for 24 h

higher spatial resolution are desirable. As already noted above, X-ray microscopy is a promising approach here, especially when a fluorescence detection option is included.

To get a impression of what kind of applications are possible, a bio-medical sample system recently measured with the AnImaX experiment shall be described by way of example.

Transport of lipids in adipose tissue of mice The bio-chemical mechanisms governing the transport of lipids from blood vessels into the brown adipose tissue of mammals is not yet understood in detail. Better insight into the involved parameters is expected to yield relevant information to understand and, on the long run, treat metabolic diseases, as e.g. diabetes, efficiently.

In the measurements at hand, the question concerned the dependency of the lipid transport from the environmental temperature under which the organism lives. As a model system mice where chosen. During their lifetime they each got a injection of lipoproteins enriched with Super Paramagnetic Iron Oxide (SPIO) nano-particles, which were supposed to serve as a fluorescence marker. Two groups of mice were kept under different environmental conditions before extracting tissue samples from their necks. One group at 4 °C, the other at 24 °C, each for 24 h.

The tissue samples were sliced into 4 μm thick slices, dried and fixated with 2.5 % formaldehyde on Si₃N₄ widows of 100 nm thickness.

It was expected that the environmental temperature leads to a stronger metabolism at low temperatures and thus a higher concentration of SPIO marked lipids in the tissue. Therefore the fluorescence measurements mainly aimed at identifying the iron in the SPIO particles and make co-localization in the cell structure visible. A varying number of particles per area depending on the temperature would serve as evidence for this theory.

To allow for iron fluorescence, the excitation energy of 1 keV was chosen above (and close to) the Fe L-edge (0.705 keV). The nominal SPIO particle size was given as 100 nm, but agglomerations of the attached lipids were to be expected.

In Figure 1.5 a 40x40 μm fluorescence scan of each sample group measured with the AnImaX setup is depicted. The scan step size was 100 nm, the exposure time per pixel 50 ms in continuous scan mode. The cell-structure of the tissue is visible in the fluorescence as well as in the transmission image. The fluorescence image furthermore shows single iron hot-spots. Before the measurement of the low-temperature sample (a), a measurement of a smaller area 20x20 μm was repeated 3 times at the left hand side of the presented scan, to yield better statistics and verify the reproducibility of the scan. The region matching the area measured before is a little darker which indicates already starting radiation damage on the sample.

The scans show that it was possible to detect the iron in SPIO agglomerations even at the low concentration at hand. The comparison of the two sample groups (Figure 1.5 (a) and (b)) nevertheless does not show a significant difference in the number of SPIO-marked lipids deposited in the tissue. Since the scans only covered a comparably small sample area, this is not necessarily evidence against the bio-medical model of the transport mechanism, but rather calls for larger scan areas and statistics. Furthermore it would be necessary to compare the results of several sample sets, before a clear conclusion could be drawn.

Nevertheless, these measurements prove the general possibility to detect even low iron concentrations in fluorescence imaging with short measurement times per scan point.

The beam damage visible in Figure 1.5 (a) furthermore illustrates the importance of short exposure times for biological samples. Freezing the sample and measuring it at a cryogenic sample stage would greatly improve the sample stability here.

Chapter 2

X-Ray Fluorescence Theory

When light (photons) passes through matter it can either be scattered, absorbed or pass without interaction (transmission). Which excitation and relaxation path is taken, is a stochastic process and depends on the atomic number Z of the material, the energy E and is commonly described by the interaction cross section ω . For X-rays the (inner) photoelectric effect and Compton/Rayleigh scattering are most likely. The phenomenon called fluorescence is one of the possible relaxation paths following the absorption of a photon. Auger electron generation and scattering processes as competing phenomena will not be described here. Please refer to [3] for a detailed description.

The probability that a photon of energy E is absorbed is proportional to the thickness z , density ρ and absorption cross section σ of the material it passes. The intensity $I(z)$ at the depth z below the surface is decreasing exponentially. The total attenuation includes scattering and ionization processes of the incident intensity I_0 and is described by the Beer-Lambert-Law:

$$I(z, E) = I_0(E) e^{-\rho\sigma(E)z} = I_0(E) e^{-\mu(E)z} \quad (2.1)$$

When radiation of energy $E = \frac{hc}{\lambda}$ is photo-ionizing an atom of element Z it causes the excitation of the electron shell or nucleus. To excite the nucleus, energies in the range of MeV are necessary. In the following energies only up to 5 keV are considered, therefore nuclear reactions can be neglected.

The energy of X-rays is high enough to excite inner shell electrons (e.g. K, L, M shell) over their binding energy E_j and thus create vacancies which are rapidly filled with electrons from a higher shell i , to regain an energetically favorable atomic state (fig. 2.2). The relaxing electron emits its surplus energy $E_{char} = E_i - E_j$ in form of a photon leaving the atom or non-radiatively excites another electron (Auger process). If a photon is generated and it is

not absorbed in the rest of sample (called self-absorption) it can be detected. This phenomenon is one of the relaxation channels for the inner photoelectric effect.

Since the energy differences between the electron shells are characteristic for each element, the energy of the emitted photon is called characteristic fluorescence line energy. The uncertainty of these fluorescence energies is fundamentally limited by the natural linewidth ΔE_{nat} , which originates in the Heisenberg energy-time-uncertainty relation and thus is coupled to the live time of the excited atomic state.

Although the natural linewidth is the fundamental limit, the fluorescence lines experience already in the sample broadening by different mechanisms. The most prominent for X-Ray fluorescence in solids are pressure broadening and inhomogeneous broadening due to surfaces or grain boundaries. Additionally, the detection of the fluorescence radiation introduces further broadening by statistical detector effects and noise. Thus the measured fluorescence lines, which originally have a Lorentz shape, are most commonly described by a Gaussian profile.

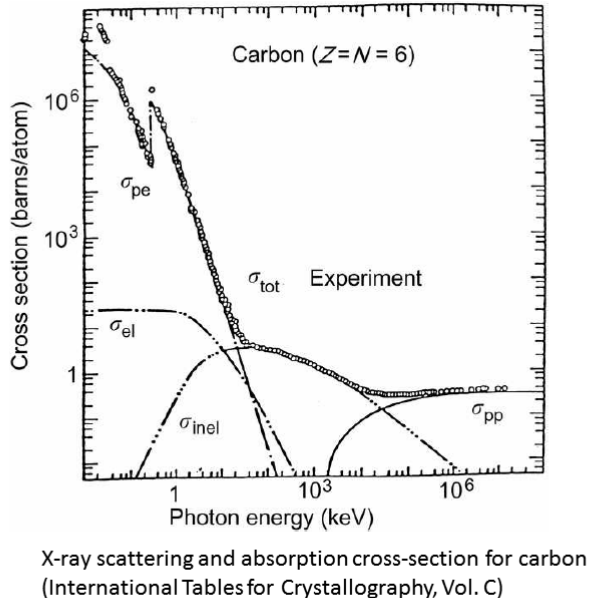
As stated above, besides the emission of a fluorescence photon also non-radiative transitions can occur when an inner shell electron is excited over its binding energy. In the Auger process, the initial inner shell vacancy is also filled by an outer electron, but instead the generated energy is not emitted as a photon but rather excites another electron over its binding energy which can leave the sample, if its remaining kinetic energy exceeds the work function of the material.

2.1 The Fundamental Parameter Approach - Sherman Equation

X-ray fluorescence (XRF) measurements use the possibility to associate the characteristic fluorescence lines with the emitting element to analyze the elemental composition of the sample. For compound samples this is not a trivial task because the different elements influence the line intensities of each other by absorption and enhancement effects.

The first theoretical description of the fluorescence intensity based on fundamental atomic parameters was presented by Jacob Sherman in 1955 [16] and further developed by Toshio Shiraiwa and Nobukatsu Fujino 1966 [17].

In the following a brief overview over the used assumptions and the resulting formulas is given.



X-ray scattering and absorption cross-section for carbon
(International Tables for Crystallography, Vol. C)

Figure 2.1: Scattering and absorption cross section of carbon. The subscripts mean: pe = photoelectric, el = elastic, inel = inelastic, pp = pair production, tot = total (from [12]).

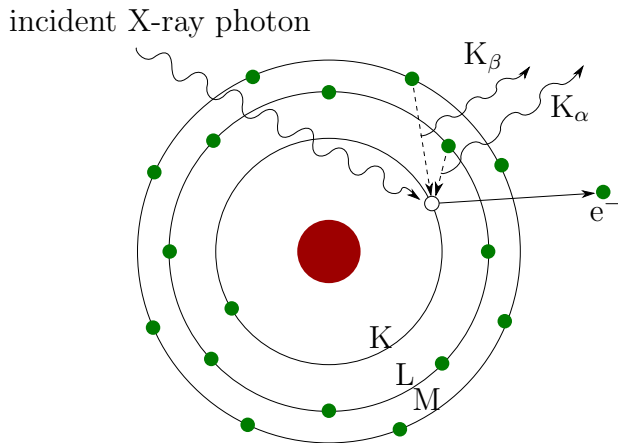


Figure 2.2: Illustration of the generation of fluorescence photons (in the Bohr model). The incident X-ray photon excites an inner shell electron and the generated vacancy is rapidly filled with an electron from a higher shell. The surplus energy is emitted as a photon with a characteristic energy.

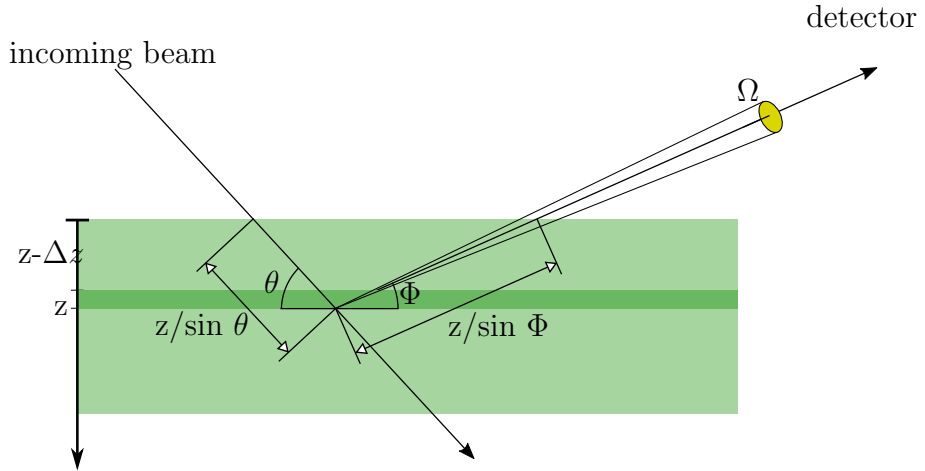


Figure 2.3: Illustration of the angles and distances inside a bulk sample.

2.1.1 Bulk Samples

Assume the following experimental situation: a monochromatic X-ray beam of intensity I_0 and energy $E_\lambda = \frac{hc}{\lambda}$ penetrates a sample under the angle θ . The element k emits fluorescence photons of energy E_j (j refers to the fluorescence line), which are detected under the observation angle Φ .

The following assumptions need to be fulfilled:

1. narrow beam assumption: the incident radiation is well collimated (parallel beam) and the solid angle of detection is small compared to the distances, so θ and Φ can be considered constant
2. the sample is infinitely thick (bulk)
3. the incident energy E_λ is smaller than 50 keV so the photoelectric effect is dominant
4. scattering is only taken into account in the total absorption coefficient
5. the sample is perfectly homogeneous and consists of elements with the atomic number Z_k and concentration C_k , where $\sum_k C_k = 1$
6. the sample surface is flat and smooth

When the beam enters the sample, it is absorbed following the Beer-Lambert Law (2.1). Only the fraction

$$I(z) = I_0 e^{-\mu_\lambda \frac{z}{\sin \theta}} \quad (2.2)$$

reaches a layer of thickness dz in the depth z underneath the sample surface. Note that all distances are mass distances (unit [g/cm^2]) and the mass attenuation coefficient refers to $\mu = \sigma\rho$, where σ is the attenuation coefficient and ρ the mass density. Furthermore $\mu_\lambda = \sum_k C_k \mu_{k\lambda}$ is the overall absorption coefficient for the mixture at energy E_λ .

Element k in layer dz absorbs radiation of the intensity

$$dI = I(z) \cdot \frac{C_k \mu_{k\lambda}}{\sin \theta} dz \quad (2.3)$$

and emits fluorescence radiation with the intensity

$$dP_k = I(z) \frac{C_k \omega_k \mu_{k\lambda} (1 - \frac{1}{r_j})}{\sin \theta} dz = I(z) \tau_{j\lambda} dz \quad (2.4)$$

where ω_k is the fluorescence yield of element k , r_j is the absorption jump ratio of the absorption edge j of element k and $\tau_{j\lambda}$ is called the emission coefficient.

Note that the notation Sherman originally used isn't commonly used anymore. Especially his definition of τ and μ differs from the definition e.g. de Boer [8] uses later. To avoid confusion, in the following all equations will follow the standard notation used today:

- index k refers to the chemical element
- index $j(k)$ refers to a certain fluorescence line j of element k
- λ refers to the incident wavelength
- $\tau_{k\lambda}$ describes the photoelectric part of the mass absorption coefficient for element k at wavelength λ .
- $\mu_\lambda = \sum_k C_k \mu_{k\lambda}$ is the overall mass attenuation coefficient (unit [cm^2/g]) of the material composed of the elements k in concentration C_k at wavelength λ . The mass absorption coefficient of each element at wavelength λ is $\mu_{k\lambda}$. This includes photoelectric interaction as well as Rayleigh and Compton scattering.
- $\epsilon_{j(k)}$ is the excitation factor of the considered line j of element k . for example $\epsilon_K = J_K \omega_K g_{K\alpha}$ for the K_α -line, where J_K is the absorption jump factor at the K-edge, ω_K the fluorescence yield and $g_{K\alpha}$ the relative emission rate of K_α relative to the other K-lines.

- To account for polychromatic incident radiation, the intensity $I(\lambda)$ is in the following assumed to be a function of the energy/wavelength. Sherman only considered monochromatic excitation. By dropping this assumption an additional integration over the wavelength is necessary.

The equation above thus can be rewritten in the common notation as:

$$dP_{j(k)} = C_k I(z, \lambda) \tau_{j\lambda} \epsilon_{j(k)} dz \quad (2.5)$$

$$= C_k I(\lambda) \exp \left[-\left(\frac{\mu_\lambda}{\sin \theta} + \frac{\mu_{j(k)}}{\sin \Phi} \right) z \right] \tau_{k\lambda} \epsilon_{j(k)} dz d\lambda \quad (2.6)$$

The fluorescence radiation generated in each infinitesimal thin layer dz is emitted isotropically ($\Omega_{max} = 4\pi$) from its source point and attenuated by the surrounding matter according to (2.1) before leaving the sample and being detected under the angle Φ . In contrast to the isotropic emission, the detector covers only a small angular interval around Φ , the solid angle Ω . Therefore only the fraction $\frac{\Omega}{4\pi}$ of the primary fluorescence is detected. The integral for primary fluorescence thus has the form:

$$P_{j(k)} = C_k \frac{\Omega}{4\pi} \int_{\lambda_0}^{\lambda_1} \int_0^\infty I(\lambda) d\lambda \cdot \exp \left[-\left(\frac{\mu_\lambda}{\sin \theta} + \frac{\mu_{j(k)}}{\sin \Phi} \right) z \right] \tau_{k\lambda} \epsilon_{j(k)} \frac{dz}{\sin \theta} \quad (2.7)$$

The primary fluorescence itself can excite other atoms in the sample. The radiation generated in the following relaxation process is referred to as secondary fluorescence and can occur in any layer dz_2 in a depth z_2 below or above z .

It was found, that secondary fluorescence can contribute up to 30 % to the detected signal in samples with a dense matrix ([4], page 322). In general it is an important effect to consider.

Nevertheless, for samples from the life sciences which normally consist of a light matrix mainly containing H, C, N and O, the secondary fluorescence contribution is much smaller and can often be neglected. For the sake of completeness the formula for secondary fluorescence as developed by de Boer [8] will be given but not discussed in detail.

The number of photons emitted by element k due to excitation by primary fluorescence from element l is:

$$S_{k,l}(E_\lambda, C) = \frac{1}{2} C_l \epsilon_l \frac{\tau_{l\lambda} \tau_{kl}}{\tau_{k\lambda} \tau_l} L P_k(E_\lambda) \quad (2.8)$$

L describes the attenuation due to the paths of the radiation through the sample and is dependent of the angles, the thickness and the mass absorption

coefficient in the sample for the incident energy E_λ and fluorescence lines $j(k)$ and l . For an infinitely thick bulk sample it is

$$L = \frac{\mu_l \sin \theta}{\mu_\lambda} \ln \left(1 + \frac{\mu_\lambda}{\mu_l \sin \theta} \right) + \frac{\mu_l \sin \Phi}{\mu_{j(k)}} \ln \left(1 + \frac{\mu_{j(k)}}{\mu_l \sin \Phi} \right) \quad (2.9)$$

The overall fluorescence intensity for the fluorescence line $j(k)$ is the sum of primary and secondary fluorescence (neglect higher order and scattering phenomena):

$$I_{j(k)} j(E_\lambda, C) = P_{j(k)}(E_\lambda, C) + \sum_l S_{kl}(E_\lambda, C) \quad (2.10)$$

2.1.2 Layered Samples

Especially in applications from the industry, where e.g. coatings or multi-layer stacks are considered, the samples consist of a number of layers on top of each other. For simplification a laterally constant layer thickness and sharp interfaces are assumed for the theoretical description. The calculation of the fluorescence intensities from each element is then not only dependent on the concentration of the element, the incident energy and the matrix composition but also on the layer thickness and stacking order. De Boer [9] develops the resulting integrals for primary and secondary fluorescence based on the case analysis of upward and downward emission inside the sample. The description accounts for absorption effects of upper layers, isotropic fluorescence emission and in-sample excitation.

Chapter 3

Motivation for a large Solid Angle Approach

3.1 Solid Angle

Assuming a point source, the solid angle Ω of a detector is defined as the projected area S of the detector active area onto the surface of a sphere with radius R completely enclosing that active area, where the center of that sphere equals the position of the point source.

$$\Omega = \frac{S}{R^2} \quad (3.1)$$

The full solid angle $\Omega_{max} = 4\pi$ would only be achieved if the detector encloses the point source completely.

Conventional fluorescence detection setups often use a detector with a circular active area of radius r_a positioned tangentially to the signal source in a distance d , i.e. the normal vector of the detector active area points to the fluorescence source point (see Figure 3.1).

For these constellations the solid angle can be calculated analytically [19]:

$$\Omega = (1 - f_s) \cdot 2\pi \cdot \left(\frac{r_a^2 + d^2 - d\sqrt{r_a^2 + d^2}}{r_a^2 + d^2} \right) \quad (3.2)$$

The factor $f_s \in [0, 1[$ describes the reduction of the active area by obstacles in the beam path, e.g. stabilization grids on the detector surface.

For non-tangential positioned detectors, the active area needs to be projected accordingly. This results in a further reduction of the solid angle.

Following the Sherman equation (2.7) the measured fluorescence intensity is

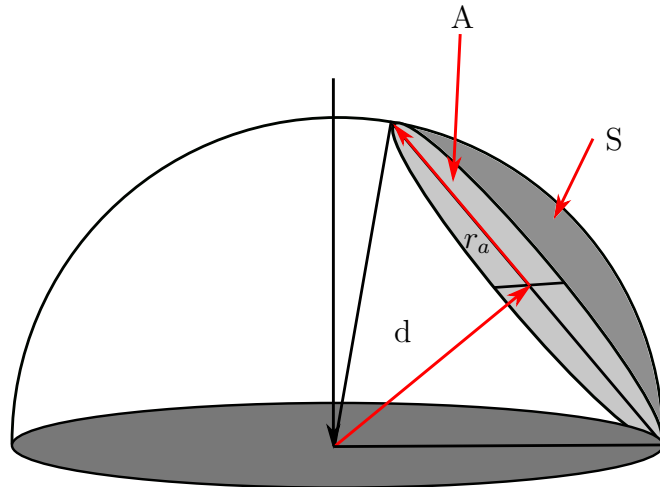


Figure 3.1: Illustration of the solid angle of a circular detector positioned tangentially to the source spot (from [19]).

linearly dependent on the solid angle of the detector, a large solid angle is therefore favorable to reduce measurement times and improve signal quality.

3.2 Incident and Observation Angle Variation: Literature Review

A large solid angle of detection is directly associated with a variation of the observation angle. In the original publication of Sherman from 1955, the equation (2.7) is derived assuming that “the entrance and exit beams may be considered well collimated (in particular the window of the detector subtends a small angle at the radiator), and hence may be treated according to ‘narrow beam’ theory” (see [16], consideration (2)).

This restriction can be interpreted as a ‘parallel beam’ approximation, resulting in a well defined incident and detection angle, or phrased differently, a small divergence and solid angle of detection.

Sherman notes that if this assumption is not fulfilled, the divergent beam “changes the functions in the integrand from exponential e^{-x} , to integral-exponential, where E_1 and E_2 apply to absorption and transmission effects respectively” [16]. He mainly focuses on an incident divergence, but his consideration is also valid for the absorption on the way out of the sample. For the specific case of the mean intensity of fluorescence radiation emitted

isotropically over the full solid angle 4π the formula changes to

$$I(l) = \tau dl \int_0^{\pi/2} e^{-\mu l / \cos \beta} \frac{\sin \beta}{\cos \beta} d\beta \quad (3.3)$$

The integral-exponential E_n has the general form

$$E_n(t) = \int_1^\infty e^{-tx} x^{-n} dx \quad (3.4)$$

which is only valid for $t > 0$. Thus using the substitution $x = \sec \beta = 1 / \cos \beta$ the emitted intensity can be written as

$$I(l) = \tau E_1(\mu l) dl \quad (3.5)$$

in contrast to the narrow beam form for the incident angle θ

$$I(l) = \frac{\tau}{\cos \theta} e^{-\mu l / \cos \theta} dl \quad (3.6)$$

Sherman already notes, but does not further develop, this approach in his paper from 1955.

In 1979 Pavlinsky and Kitov [15] presented a correction approach for divergent illumination of homogeneous samples and described the effects of the source shape (circular, linear, point) on the fluorescence intensity. The developed formula is valid for a large spot on a homogeneous sample. They focused on the effects on the efficiency of the fluorescence radiation excitation and suggested an effective incident angle.

In 1994 Chang and Wittry [7] discussed the effects of a non-parallel incident beam on the fundamental parameter equations. Namely they deal with convergent beams which occur when the incident beam is focused on the sample surface and thus becomes divergent inside the sample. They use a power series expansion to approximate the involved area integral and thereby develop an analytical form of the Sherman equation for primary and secondary fluorescence. Since their study is motivated by laboratory setups with rectangular crystal diffractometers as focusing optics, a rectangular beam footprint is assumed. They found a deviation of the fluorescence intensity relative to the parallel beam case of up to 8% for incident angles between 50°-90° and divergent angles 4°-16° for CrFe and NiFe samples.

The consequences of a non-parallel beam in the excitation and/or detection path have been further examined by Malzer and Kanngießer in 2003 [13]

with a Monte-Carlo based calculation approach. They concentrated on homogeneous samples and suggested a equivalent angle model, in which certain experimental configurations (incident angle θ , divergence angle α , observation angle Φ , solid angle of detection Ω) are assigned with equivalent configurations assuming ‘narrow beams’ ($\alpha = 0$, $\Omega \approx 0$). These equivalent angles result from a fit to the results obtained by Monte Carlo (MC) calculations for varying factors $\mu\rho D$.

It was shown that the results calculated with these equivalent angles only show slight deviation from the MC results over a wide range of parameters $\mu\rho D$. Equivalent angles are thus a promising approach to correct the FP calculations for non-parallel beam setups and homogeneous samples. In Section 6.3.1 this approach is further discussed.

In 2004, Mantler and Kawhara [14] noted that varying observation angles can cause different detector response functions, if an energy dispersive detector is used. Furthermore they give an approximation of the relative error introduced by a polychromatic beam with a divergence of $45^\circ \pm 10^\circ$ on a stainless steel sample in the 0.1 % range for K-lines and up to 1 % for L-lines.

Bonizzoni et al. (2006, [5]) further looked into the effects an uneven sample surface and thus a non-constant incident/observation angle have on FP calculations. They derive an expression for a correction factor Q_{ik} which is dependent on the excitation energy E_k and fluorescence line energy E_i .

They also address the issue of solid angle variation with depth in the case of equal incident and observation angle (illumination/detection perpendicular to the surface). They give an approximation of the introduced relative error C_{ik} of $<1\%$ for distances in the centimeter regime. The formula they derive is strictly speaking only valid for isotropically emitting radiation sources and infinity thick samples. They conclude that the irregular surface effects are smallest in this configuration whereas the solid angle effects gain importance. It has to be noted that the decrease in distance d increases this factor $\mathcal{O}(1/d)$ (for directed beam illumination as found at synchrotrons). For a compact setup the solid angle variation therefore becomes a error source which is worth further examination.

Although the problem of divergent angles and explicitly large solid angles of detection has been researched with various approaches ever since Sherman published his article in 1955, no full analytical incorporation of divergent angles into the Sherman equation has been published or adopted by standard quantification algorithms yet. The named sources show that even for homogeneous samples this introduces an additional error to fundamental pa-

rameter calculations which often is not accounted for.

3.3 Inhomogeneous Samples

The studies mentioned above so far all assume a homogeneous sample and often only treat primary fluorescence.

For layered samples and/or lateral inhomogeneities the variation of the absorption path in the sample with varying angles was not yet formulated in a closed analytical form. The necessary knowledge about the sample layout and composition makes full backward calculations for quantification in real experiments probably impossible.

Nevertheless the assumption of a homogeneous sample is untenable for microscopy applications where exactly the lateral change of composition is the interesting feature to examine.

Although full backward calculations will never be possible without additional knowledge about the sample, it is possible to simulate the fluorescence spectra of inhomogeneous samples. Conventionally two possible approaches are at hand: Monte Carlo calculations or direct ray tracing. Both of them are statistical methods which need to be treated numerically and require rather long simulation times.

Such simulations can be a viable tool to study what kind of effects can occur in different sample types and to cross-check measurement data with assumptions about the sample. Furthermore they can help to estimate which sample properties are accessible for measurements in certain setups. Expectable effects are for example:

- shadow effects e.g. at surface structures or inhomogeneities
- unknown information depth for thicker samples
- overlapping of shadow effects and beam footprint blurring (loss of spatial resolution)
- contribution to the error in the calculated elemental concentrations (unaccounted self-absorption)

In contrast to the stochastic approaches named above, we suggest a new fundamental parameter based approach combined with discrete geometrical path length calculations.

3.4 Implications of Large Solid Angles on Spatial Resolution

As mentioned in Section 1.5, the theoretical and experimental determination of the spatial resolution traditionally deals with full field optical microscopy. In scanning (transmission) techniques, the resolution is not only determined by the used wavelength and the numerical aperture of the used optics, but also by scan step size, focus size and detector area/distance.

Some methods, as ptychography, make active use of the possibility of oversampling (here: overlap of the illuminated sample area of neighboring scan steps) to computationally increase the resolution.

Concerning fluorescence imaging it has to be kept in mind that the detected radiation is isotropically emitted by the atoms of the sample. A diffraction based approach as Abbe used, is therefore not applicable, but rather a point source model as used by Rayleigh. Additionally the information is not independent of the rest of the sample, absorption and higher order fluorescence effects make it highly non-trivial to define the actual source of the detected radiation. A theoretical determination of the resolution is therefore difficult and scanning fluorescence measurements in a traditional, small solid angle setup, are in the simple view considered to be mainly limited by the spot size of the incoming beam on the sample.

Looking closer on the paths of the incoming photons in the sample, it is apparent that even this assumption tends to overestimate the resolution. Since real samples have a certain thickness and are often not homogeneous throughout this thickness, it is an open question on how to evaluate the information depth. Each depth in the sample is excited by a different intensity and the paths of the fluorescence photons are highly variable. Secondary fluorescence can therefore originate from a different volume than primary fluorescence. Nevertheless these effects are normally small in thin samples and when measured at small solid angles.

As a large solid angle detector is used, the shadow and absorption effects mentioned in Section 3.3 can contribute to a loss of spatial resolution in fluorescence imaging. The distinction between internal absorption effects and actual changes in the sample structure and/or composition are not trivial. Originally sharp edges might result in intensity gradients of certain fluorescence lines. The determination of the spatial resolution by evaluating the intensity contrast thus loses its significance. Combined with the question of the visible information depth, every resolution value needs to be handled with care. Even in small solid angle setups, it is common to only speak of

smallest visible structures instead of resolution.

3.5 Quantitative Imaging

Quantitative X-ray fluorescence analysis generally refers to point measurements on homogeneous samples. As described above inhomogeneities and short measurement times per point as typical for imaging have serious implications for the reliability and accuracy of quantification.

For homogeneous and layered samples the most common quantitative approach is the fundamental parameter based backward calculation from fluorescence intensities to concentrations using reference samples for the calibration of the detector and experiment geometry.

To allow for this kind of calculations the setup needs to be well known and an initial guess for the composition and/or sample properties as e.g. layer thicknesses is favorable. The calibration of the energy axis must be performed with considerable care and the measured spectrum needs to be deconvoluted according to the expected elements. Detector artifacts, background contributions and scattering effects need to be corrected for before applying a suitable fit algorithm.

Reference free quantification is only possible if the detector is calibrated absolutely and the setup (geometry, optical properties) is well characterized. Therefore reference-free quantification is uncommon and only done at metrology institutes like the Physikalisch Technische Bundesanstalt (PTB).

The deconvolution and fitting of the spectrum to fundamental parameter based theoretical curves can be done by using free software packages like PyMCA, developed by Amando Solé at ESRF (Grenoble, France). This software also allows for the batch fitting of mapping data.

Since fluorescence signals in the soft energy range are rather weak, the spectra for each measurement point often do not have a good signal-to-noise ratio. The calculated fluorescence intensities thus have a rather high uncertainty. Therefore the backwards calculation is generally prone to high errors in this energy regime and often fluorescence imaging data is only presented qualitatively (as intensities).

Since the Sherman equation assumes either a homogeneous sample or at least a fixed layering for the calculation of the fluorescence intensities, the same must be true by a FP based backward calculations. For layered samples it is furthermore necessary to fit to an initial model of the layer order and thicknesses.

For inhomogeneous samples as common in imaging applications often a local homogeneity is assumed. If this assumption is valid depends strongly on

the sample at hand, the focus size and the scan parameters. Even if the assumption is justified, the used algorithms depend on the applicability of the Sherman equation itself. As discussed in Section 3.2 there is not yet a suggestion how to analytically incorporate wide angular ranges into the equation. It is even questionable what a quantification would mean in this situation. If the concentration changes in the depth of the sample but the probe integrates over the whole thickness, the information depth is hard to define. A large solid angle adds a further uncertainty (or integration) lateral to the sample surface.

Only methods which are sensitive to 3D effects can therefore be expected to make a proper quantification possible. The issue of self-absorption is therefore a current research topic in fluorescence tomography approaches. Since tomography normally aims to make thin slicing (and comparable preparation methods) unnecessary, they are challenged with achieving a high enough information depth and reasonable measurement times.

The large solid angle of the AnImaX setup thus poses a challenge for quantification, while at the same time enabling the necessary count rates for it. It would go beyond the scope of this thesis to aim at answering all the open questions associated with this situation. But a first step to understand the implications of a large solid angle for the spectra and image reconstruction is to simulate its effects. Based on these simulations, possible strategies towards quantification of fluorescence imaging data can be better evaluated.

Chapter 4

Experimental Setup: AnImaX

The AnImaX end station is a scanning transmission X-ray microscope (STXM) with an included fluorescence detector. It is designed to allow for fast nanoscale imaging in an energy range of 300-3000 eV. Available imaging options include full-field, absorption and phase contrast imaging in transmission as well as the mapping of the lateral elemental distribution from the fluorescence signal.

It was developed and build as part of the BMBF project FlexIX and its follow-up AnImaX as a cooperation of the TU Berlin and the University of Applied Science Koblenz (see [2]).

Although designed for the P04 beamline at Petra III (DESY Hamburg), it is flexible enough to be used at other synchrotron beamlines with a similar energy range (as for example BESSY II).

The arrangement of the used optical elements is represented in Figure 4.1. The beam coming from the beamline (right side of Figure 4.1) enters the first measurement chamber, which is empty and serves as a differential pumping volume to bridge the ultra high vacuum ($\approx 10^{-9}$ mbar) in the beamline and the high vacuum ($\approx 10^{-6}$ mbar) in the second measurement chamber, which is only connected through a small diameter flange.

In the main chamber, the beam is focused by a Fresnel zone plate with a diameter of 333 μm , an outer zone width of 40 nm and has a central stop of 160 μm diameter. In a distance of about 2/3 of the focal length a circular pinhole is used as an order sorting aperture (OSA) with a diameter of 150 μm . Since the focal length of the used zone plate is about 7 mm the OSA is fixed with a small metal tube together with the zone plate to a piezoelectric motor driven stage and can be inserted into the central hole of the QUAD detector. The focused beam thus passes trough the hole in the detector before hitting the sample.

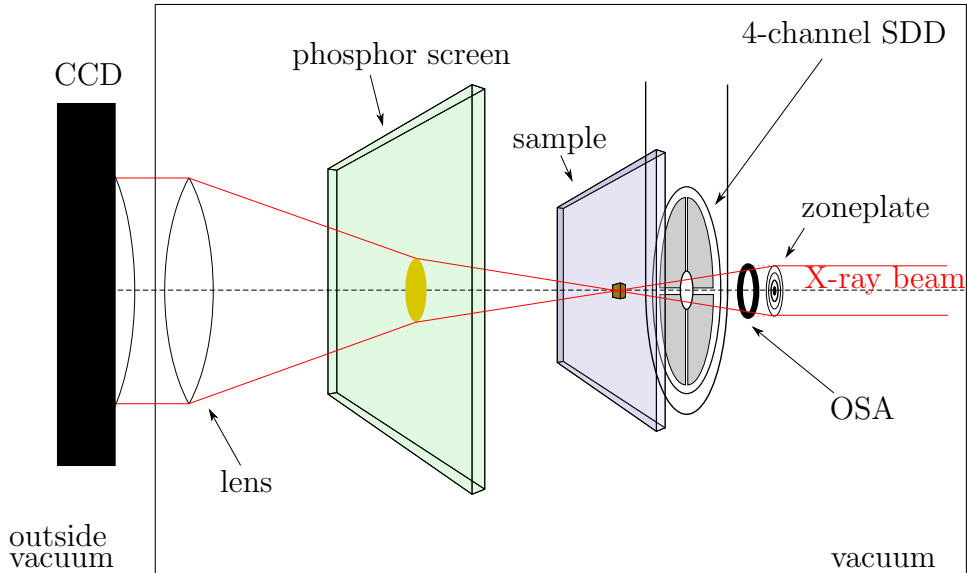


Figure 4.1: Illustration of the AnImaX experimental setup

The sample is fixed to a sample frame which itself is fixed to a scanner frame. The scanner frame (and thereby the sample) can be moved in x (horizontally), y (vertically) and z (in beam direction) for focusing and orientation on the sample. The sample frame itself is only movable in x and y by encoded piezoelectric crawlers, with a position accuracy of 0.1 nm and a total range of 100 μm . The range and accuracy of the sample frame are decisive for the scan area and resolution. To make fast changes between samples possible, up to 5 samples can be positioned on the same sample holder.

The sample frame is connected with a computer controlled scanning unit, which allows step-by-step scanning as well as on-the-fly scanning with permanent data acquisition. The on-the-fly mode allows for a considerable reduction of the scan time. A large scan of 250x250 px with 200 ms measurement time per point thus only takes about 4 h.

A phosphorous screen behind the sample is excited by the transmitted X-rays and emits light in the visible regime (green), which is then collected by a optical lens and detected by a fast readout CCD camera outside the vacuum chamber.

4.1 The new QUAD Detector

The QUAD detector by Bruker is an unique 4-channel SDD with a special geometry: 4 independent kidney-shaped SDD cells are arranged like a

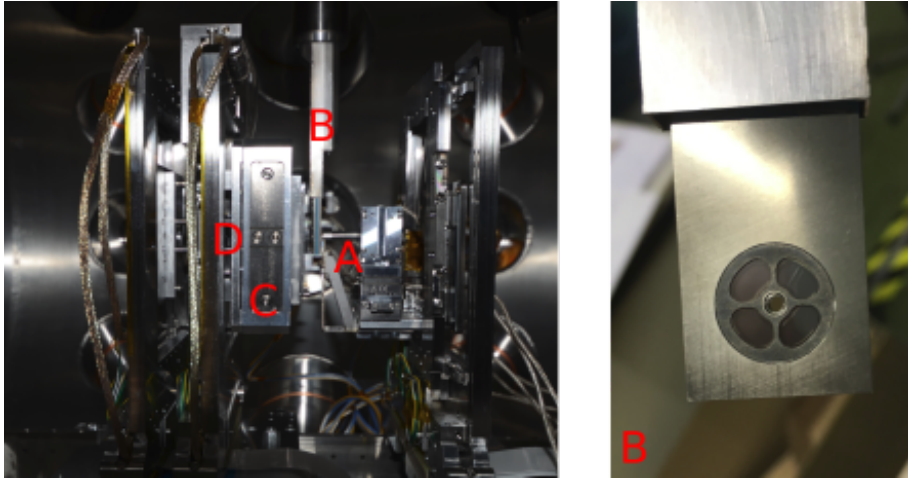


Figure 4.2: Photo of the AnImaX end station and the QUAD detector. A) Fresnel zone plate and OSA on a tube shaped support, B) QUAD detector (side view), C) sample on manipulator stage, D) phosphor screen and optical lens (not visible on the image). The 4 kidney shaped detector cells and the central hole are readily identifiable on the right hand image. This side of the detector would be orientated facing the sample.

cloverleaf around a central pinhole through which the excitation beam passes before hitting the sample. Each SDD cell has an active area of about 15 mm^2 resulting in an overall active area of 60 mm^2 .

To shield the silicon chip from photo electrons, it is equipped with a $0.5 \mu\text{m}$ thick Mylar window. Due to this comparably thin window, low energy photons can still be detected. Electrons up to about 3 keV are trapped, which limits the effective energy range to the high energy side (for the functional principle of SDDs see chapter 1.4).

Due to its ring like shape (see Figure 4.3) the solid angle of detection can be calculated with the formula for circular detectors (3.2) as the difference of the solid angle of the outer radius r_a and the inner radius r_i [19]:

$$\Omega(d) = 2\pi(1 - f_s) \left(\frac{r_a^2 + d^2 - d\sqrt{r_a^2 + d^2}}{r_a^2 + d^2} - \frac{r_i^2 + d^2 - d\sqrt{r_i^2 + d^2}}{r_i^2 + d^2} \right) \quad (4.1)$$

This function has a global maximum at a certain distance d_{opt} and only varies slightly in a intervall of $\pm\Delta d$ around this value. It is therefore favorable to position the detector within this distance intervall to the sample surface.

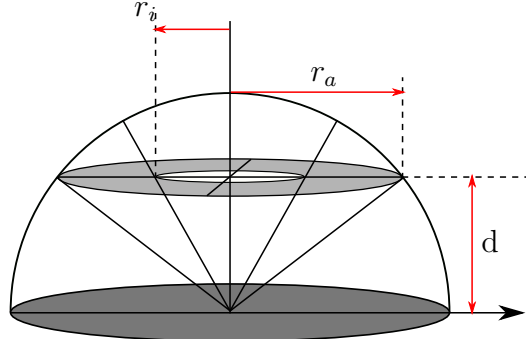


Figure 4.3: Illustration of the solid angle of an annular detector parallel to the sample surface (from [19]).

Since the metal frame which defines the distance d between sample and detector in the experiment has a z-offset to the actual silicon chip, the inner and outer detector radii are themselves functions of the distance d . The nominal radii defined by the metal frame need to be projected to the chip following the equations (see Figure 4.4)

$$r_i(d) = \frac{d + d_{Si}}{d + d_{uE}} \cdot r_{i,nom} \quad (4.2)$$

$$r_a(d) = \frac{d + d_{Si}}{d + d_{lE}} \cdot r_{a,nom} \quad (4.3)$$

Minimizing (4.1) gives the respective $d_{opt} = 1.42$ mm for a nominal value of $r_{i,nom}$ and $r_{a,nom}$, which were provided in personal communication.

The setup is therefore designed to make this rather small distance possible and thus maximize the solid angle of detection (see Figure 4.5). For optimal positioning the theoretical maximum solid angle of detection is about 1.1 sr, if a form factor of f_s is assumed. The form factor reflects the reduction of the full-ring area by the metal support frame (kidney-shapes). For an analytically exact description, this form factor would also be distance dependent, which is neglected here.

Due to the flat maximum of the curve (4.1), the positioning of the detector can tolerate a sufficient uncertainty: the solid angle does not fall under 95 % of the maximum value for $\Delta d_- = -0.61$ mm and $\Delta d_+ = 0.86$ mm around the optimum distance d_{opt} (see Figure 4.5).

Note that conventional fluorescence setups have a solid angle of detection smaller 0.1 sr.

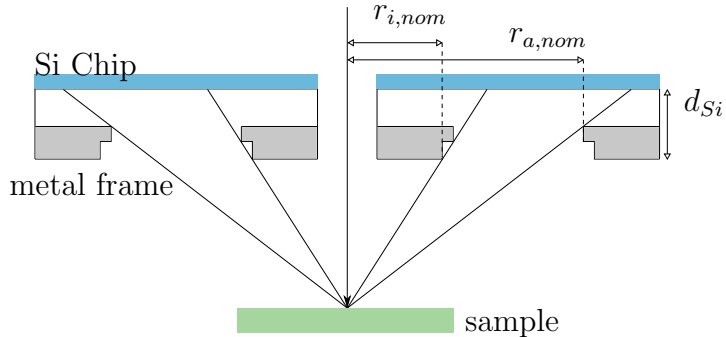


Figure 4.4: Side view of the QUAD detector showing the metal frame, simplified.

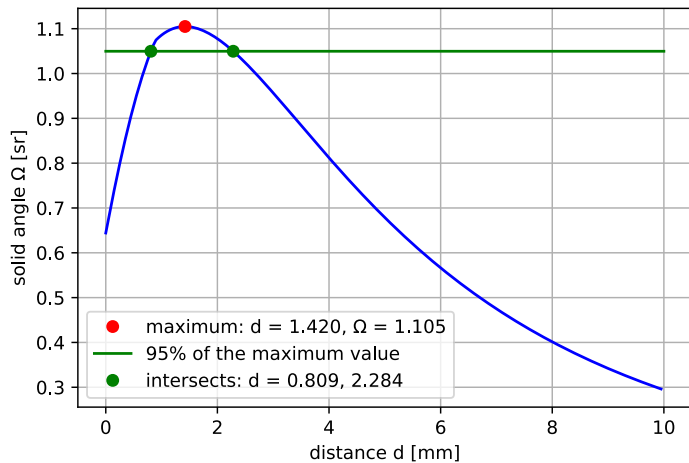


Figure 4.5: Solid angle of detection for an annular detector in dependence of the nominal distance d between sample and detector (frame) surface (see [19]). The calculation includes the distance dependence of the effective detector radii due to the metal frame. The green line and dots indicate the range of the plateau.

Chapter 5

Simulation Approach: QUADaps

To simulate the special geometry and resulting effects on fluorescence signals of inhomogeneous samples, a Python based simulation program was developed: **QUADaps** (**QUAD** absorption path simulations).

The assumptions and underlying models of this program will be described in the following chapter.

5.1 The xrfLibrary

To facilitate fundamental parameter based calculations and simulations a software package called “xrfLibrary” was developed by the AG Kanngießer (Technical University Berlin). Together with the database package “xrlfupa” containing the fundamental X-ray parameters and a database of optical parameters, it is a powerful tool to simulate various X-ray setups and measurements. The xrlfupa offers the choice between different databases (Ebel, Elam, Henke) and additional parameters measured in cooperation with the PTB Berlin. Here, only the Elam database is used.

The library was originally written in C. In the following a Python wrapper is used, which itself is still constantly developed and updated.

In general the library offers a wide range of tools including the definition of sources, specimen, filters and detectors. The different elements are themselves based on a couple of basic functions which mostly work on objects from the central class *spectrum()*.

A *spectrum()*-object consists of a continuum part and a characteristic line array, each of these arrays containing the intensities (in counts/second) at the respective energies (in keV). Moreover the characteristic line part includes

a reference to the IUPAC notation of the fluorescence line. It is important to note, that each xrfLibrary tool works on the *spectrum()* directly, which means it does not create a new object but changes the object itself. If several operations should be done with the same spectrum separately, the object itself needs to be multiplied first. In traditional cases the *spectrum()* is first generated by a source and then altered by every optical element in the setup according to its properties.

The *source()*-class contains three different source types: *monoSource(E, I)*, *arraySource(E₁, I₁, E₂, I₂, ...)* and *tubeSource(tube parameters)*. The *tubeSource()*-object generates a Bremsstrahlung spectrum with characteristic lines according to the tube properties, the other two sources only generate characteristic line spectra.

Several *filter()*-objects can be added to the beam path. They serve as attenuation filters according to their thickness (in cm). In the following only the *filterArray()* and *layerFilter()* functions were used. The specification of the material of the filter can either be done by using chemical elements and their parameters from the xrlfupa or defining a compound. If a compound is defined, the density and composition (in mass fraction) needs to be given. This makes a wide range of flexible filter designs possible.

The sample is defined as a *specimen()*-object. It can be layered or homogeneous, the composition of each layer is defined as a *compound()*. Once defined, the primary fluorescence and secondary fluorescence of the sample can be calculated depending on the incoming intensity and geometry:

$$\begin{aligned} P_{j(k)} &= C_k \frac{\Omega}{4\pi} I_\lambda \int_0^D \cdot \exp \left[-\left(\frac{\mu_\lambda}{\sin \theta} + \frac{\mu_{j(k)}}{\sin \Phi} \right) z \right] \tau_{k\lambda} \epsilon_{j(k)} \frac{dz}{\sin \theta} \\ &= C_k \frac{\Omega}{4\pi} I_\lambda \frac{\tau_{k\lambda} \epsilon_{j(k)}}{\sin \theta} \frac{1 - \exp \left[-\left(\frac{\mu_\lambda}{\sin \theta} + \frac{\mu_{j(k)}}{\sin \Phi} \right) D \right]}{\left(\frac{\mu_\lambda}{\sin \theta} + \frac{\mu_{j(k)}}{\sin \Phi} \right)} \end{aligned}$$

Note that here the distance z (perpendicular to the surface) refers to a mass distance, including the density ρ (the unit is thus $[z] = \text{g/cm}^2$), D indicates the overall thickness of the layer.

The detection of the spectrum is simulated via a *detector()*-object. This far only Si detectors are implemented in different geometries. Parameters as the efficiency, chip thickness and additional windows can be included.

An annular detector with large solid angle is not yet modeled. Therefore the simulation program described in the following section was implemented to account for the specific setup of the AnImaX microscope.

5.2 Model Assumptions

As described in section 2, the fundamental parameter approach for X-ray fluorescence divides the contribution of primary, secondary and higher order mechanisms. Since the AnImaX end station is designed for soft/tender X-ray microscopy (up to 3 keV) of light matrix samples, the following simulations are restricted to primary fluorescence effects. For this kind of experimental situation and samples the contribution of higher order fluorescence effects is small compared to the primary signal [4] and therefore only small errors may be expected by this assumption.

QUADaps assumes a narrow, parallel incident beam and thus a point excitation. Effects caused by the footprint of the beam are not accounted for. The focus achieved by the zone plate is in the range 50-500 nm which is small relative to the distances between sample/detector chip (2.4 mm) and sample/zone plate (e.g. 7 mm at 700 eV). Thus a point excitation as well as a parallel beam assumption is valid here.

These assumptions can be understood as a negligence of the following effects: For a parallel beam with an extended footprint on the sample a further blurring effect on zone borders has to be expected. A divergent incident beam would lead to a further information loss concerning the probing volume and information depth. Calculations that consider this kind of effects would probably be more efficient using statistical methods like ray tracing or Monte Carlo.

The sample is defined beforehand and consists of a number of cuboid shaped zones of different sizes and compositions.

The zone interfaces are assumed to be flat, perpendicular or parallel to the defined coordinate axes and perfectly sharp. Roughness would need to be defined explicitly in the zone definition with additional zones. Although this in principle is possible, it would result in increased simulation times and therefore is not recommended.

5.3 Simulated Sample Layout: Possibilities and Limits

Since computer simulations always need a certain level of discretization the sample layout is restricted to rectangular shapes, as already mentioned above in Section 5.2. Only sharp edges and shapes discretized to cuboids can be defined. Besides this restriction all kinds of 3 dimensional samples can be

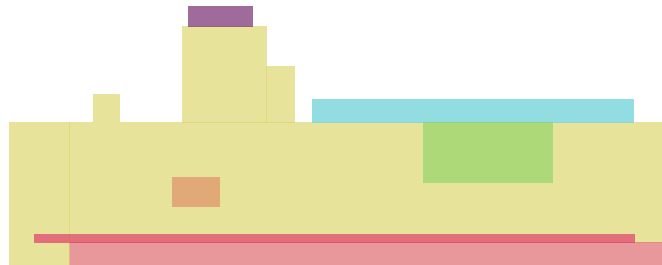


Figure 5.1: Example for possible sample layouts (crosssection): surface structures, buried particles, layers and density variations can be simulated. Only rectangular shapes and smooth zone borders are possible.

simulated, as can be seen in Figure 5.1. For holes or overhanging structures, the density of the respective cuboid can be set to zero, minimizing absorption and fluorescence. The backside of the sample is generally considered to be flat.

The simulation is restricted to primary fluorescence and light matrix samples. Otherwise the neglected secondary fluorescence contribution would result in a large simulation error.

Detector effects as described in Section 1.4 as well as signal contributions due to scattering are not implemented (except the contribution of scattering cross section to the absorption cross section, as used in the Sherman equation).

The simulation makes point measurements, line scans, as well as area mapping of a relatively free sample layout possible. It accounts for effects in 3 dimensions, as explained in Section 5.8. Moreover the incident angle can be varied (without effect on the irradiated area) as well as the size (radii) and distance of the detector.

This far only monochromatic sources can be defined, but the energy as well as the intensity can be chosen according to the experimental situation. The calculation of the fluorescence spectrum is also restricted to characteristic lines, noise is not accounted for.

5.4 The Coordinate System

In contrast to the experiment, where the sample stage is moved while the excitation beam is fixed, the coordinate system used in the simulations is fixed to the sample, not to the X-ray beam.

The common z-origin is the backside of the sample. It is always assumed as leveled and smooth. z is defined as ≥ 0 .

index	value range	description
n	$0 - N$	detector radius intervall
ϕ	$0 - \frac{\pi}{2}$	detector angular intervall
k	$0 - K$	index z-step
i	$0 - I$	x-zone index irradiated zone
g	$0 - G$	y-zone index irradiated zone
w	$0 - W$	z-layer index irradiated zone
s	$0 - I$	x-zone index absorbing zone
p	$0 - G$	y-zone index absorbing zone
j	$0 - J$	z-layer index absorbing zone (not containing current scan point (x,y))

Table 5.1: Overview of used indices for different zones and layers in the QUADaps program.

The (x, y) - plane is the lateral sample plane. It is defined as a grid with rectangular zones (i, g), which can have different sizes, but the grid-lines (or zone borders, see Figure 5.10) are defining for the whole sample plane.

Each zone is assigned a certain sample 'type' (or layer stack) which is defined by the user beforehand. Each layer stack is a xrfLibrary *layerSample()*-object. If the sample has a common support layer, this needs to be included in each layer stack definition as the last layer.

The cuboids of neighboring lateral zones do not need to have leveled heights. This means there is no general grid in z -direction (in contrast to the (x, y) - grid).

In the following the cuboid which is excited by the incoming radiation has the indices (i, g, w), whereas the cuboids through which the fluorescence radiation passes on its way out of the sample will be indicated by the indices (s, p, j). See Table 5.1 for a overview of the used indices.

5.5 Area Decomposition of the Detector

As already stated, some assumptions common in the fundamental parameter based fluorescence calculations do not hold anymore for large solid angles. A closed form analytical expression was not yet developed, therefore the following simulations are based on integrating the signal with respect to the detector area.

Since the detector has a (almost) circular shape, its area is virtually decomposed in radial and angular elements, defined by a radius r_n and an angle ϕ

(as indicated in Figure 5.2).

For each detector element the fluorescence radiation from the excitation spot at (x, y) in the depth z is modeled as a beam hitting this detector element in the center.

The definition of the virtual radii r_n follows

$$r_n = r_i + \left(n + \frac{1}{2}\right) \cdot \frac{r_a - r_i}{N_r} \quad (5.1)$$

where N describes the total number of radial detector elements. The virtual detector radii vary between the projected inner ring radius $r_i = 2.97$ mm and the outer radius $r_a = 5.66$ mm.

The detector is fixed with respect to the beam position, therefore these radii r_n are constant throughout the simulation procedure (see Figure 5.2).

The simulated 'beams' travel along different paths through the surrounding sample before reaching the detector and therefore experience a specific absorption, which is simulated by xrfLibrary *filter()*-objects.

Moreover the intensity reaching each detector element is depending on the solid angle $\Omega_{n,\phi}$ of this element. The calculation of the solid angle for an annular detector is dependent on the width of the detector ring and the distance $d(z) = d_0 - z$. The nominal distance of the detector to the backside of the sample is defined as $d_0 = \text{const.}$

The used formula is a special case of the formula for annular detectors based on the work by Zaluzec [19]. The inner radius of ring n is denoted by $r_{n,i}$, the outer by $r_{n,a}$:

$$\Omega_n(z) = 2\pi(1 - f_s) \left(\frac{r_{n,a}^2 + d(z)^2 - d(z)\sqrt{r_{n,a}^2 + d(z)^2}}{r_{n,a}^2 + d(z)^2} - \frac{r_{n,i}^2 + d(z)^2 - d(z)\sqrt{r_{n,i}^2 + d(z)^2}}{r_{n,i}^2 + d(z)^2} \right) \quad (5.2)$$

The factor f_s describes the reduction of the active detector area by the metal support frame (indicated by the darker area in Figure 5.2).

Instead of calculating the solid angle Ω for the whole detector, the solid angle for each virtual detector ring is calculated following the same equation (5.2) using the radii $r_{n,i/a}$ and a constant factor f_s .

Since the shape of each detector cell (defined by the metal frame) is not a

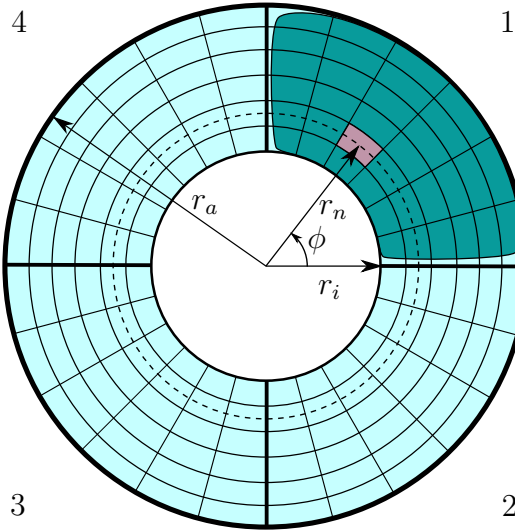


Figure 5.2: Illustration of the decomposition of the QUAD detector in radial and angular elements. The overall detector signal is calculated by summing over the respective signal in each cell. Thereby the 4 independent detector cells yield different signals due to varying absorption paths of the exiting fluorescence radiation.

perfect arc but rather a kidney, the use of a constant factor f_s for all virtual detector elements is a simplification. Nevertheless, for a first assessment the expected error is small enough to justify this assumption.

For the angular detector decomposition the solid angle of a certain ring has to be divided by the number of angle intervals N_ϕ set by the user:

$$\Omega_{n,\phi} = \frac{\Omega_n}{N_\phi} \quad (5.3)$$

The $0.5\text{ }\mu\text{m}$ Mylar window

5.6 Beam Position along Z

For each lateral scan position (x, y) the detector signal is calculated by summing over the fluorescence signal emitted from different depths z , discretized in steps of Δz .

The monochromatic source is modeled as a xrfLibrary *monoSource()*-Object with the intensity I_0 at energy E_0 . Starting from the surface of the sample at the current (x, y) position, the source spectrum excites the (virtual) sample layer (i, g, w) with the thickness h_w to emit primary fluorescence.

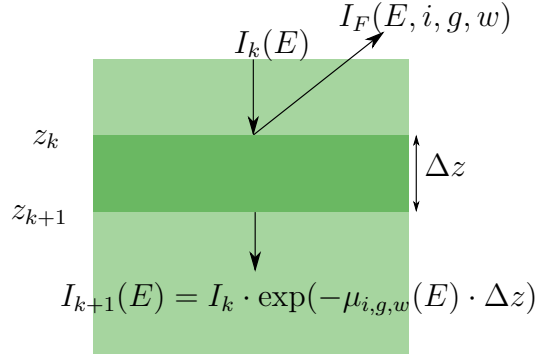


Figure 5.3: The transmission for each z-position is calculated following the Beer-Lambert-Law implemented in the *filter.transmission()* function of the xrfLibrary. The transmitted intensity serves as excitation for the calculation of the primary fluorescence of the next sample slice Δz

The transmission through this layer is modeled in steps z_k of thickness Δz . For each step k the transmission of a *filter()*-object of the thickness Δz is calculated and used as the new excitation intensity for the next z-position z_{k+1} (see Figure 5.3).

$$z_{k+1} = z_k - \Delta z \quad (5.4)$$

The distance between detector and z-iteration point is:

$$d(z_k) = d_k = d_0 - z_k \quad (5.5)$$

As an additional *break* condition for the z-iteration, it is possible to set a threshold intensity:

$$I(z_k) = I_k \geq I_{thres} \quad (5.6)$$

Since z is decreasing, $d(z)$ is growing with each iteration. If z sinks under the lower z -border z_w of the currently excited layer w , the next layer $w + 1$ is used for the calculation of the primary fluorescence signal. For thin samples the calculation is stopped as soon as the backside of the sample is reached ($z = 0$).

Please note that the step size Δz should be smaller than the thinnest layer. Otherwise it is likely that the discrete virtual beams do not intersect the small structures and certain effects are not simulated properly. This behavior is due to the discretization and would not reflect the physical reality properly. Therefore extra care needs to be taken when choosing the step width Δz .

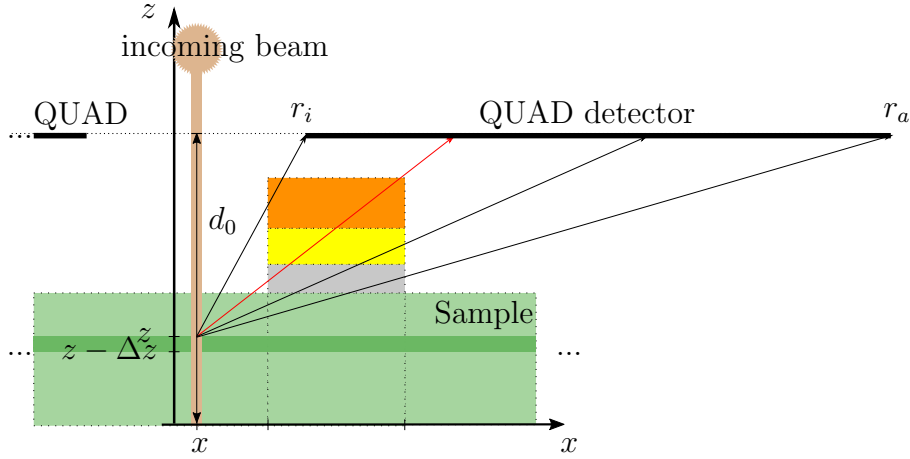


Figure 5.4: Side view of a model sample. Layers of different heights and composition (color) are stacked upon each other on a support layer. The thin black lines indicate primary-fluorescence-'beams' passing from the source spot at (x, z) through the different sample layers to the QUAD detector cell, which is represented by the thicker black line in the z -distance d_0 above the sample.

5.7 2D Considerations

The sample is designed as consisting of stacks of layers with layer thicknesses h_j . The index j is counted from 0 to $J_{s,p}$ starting from the top layer (layer closest to the detector) in the current lateral zone (s, p) . (Note: Layers in different zones can have a different j -index, although they cover the same z -interval (see Figure 5.4)).

The calculation of the detected spectrum is based on 'beams' going from the scan spot (x, y, z_k) to a certain detector element. The detector elements are defined by the detector radius r_n and the polar angle ϕ , as described under section 5.5.

When such a virtual beam passes through a layer stack, it passes the projected thicknesses of the layers, as indicated in Figure 5.4 and 5.5. For example, consider the second beam from the left (red) in Figure 5.4 and 5.5: the primary fluorescence generated in depth z by a thin layer of thickness Δz first passes through the blue zone, leaves the sample and enters the neighboring zone where it is attenuated first by the dark grey then the yellow and finally the orange layer. Each of these layers is modeled as a absorption filter for the primary fluorescence. The thicknesses of these filters need to be calculated according to the projection along the beam vector, as explained in the

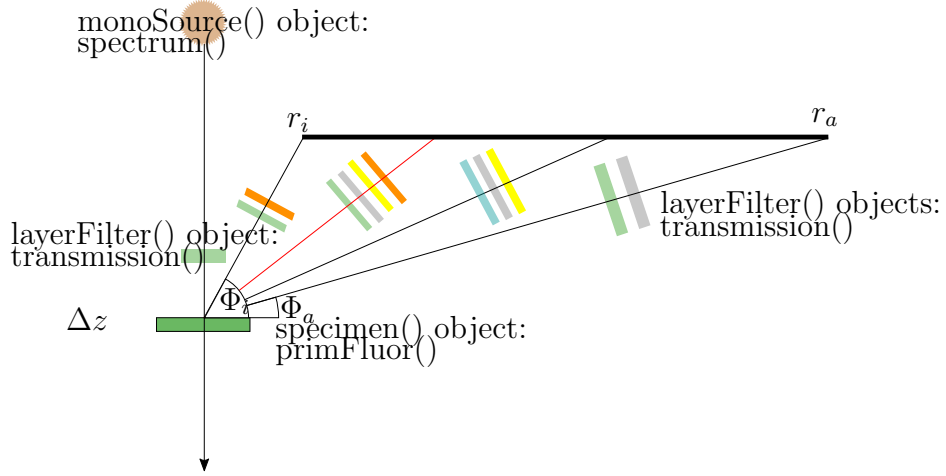


Figure 5.5: Schematic illustration of the used xrfLibrary objects for the representation of Figure 5.4 in the simulation program.

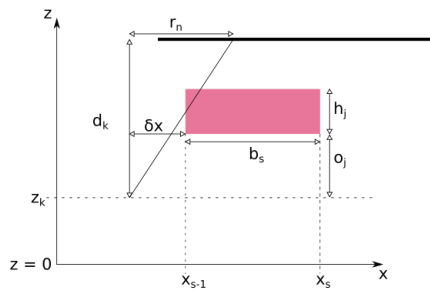
following considerations. Since fluorescence radiation is emitted isotropically from its origin at (x, y, z) the solid angle of each detector element accounts for the fraction of the primary fluorescence emitted in the virtual beam direction.

We first consider the cross section along the (x, z) -plane to illustrate the calculation of the absorption filter thicknesses. The following derivation of the necessary formulas is done by way of example for detector cell 1 (located in the positive x and positive y direction from the scan point). With an adequate adjustment of the zone indices the same considerations are applicable for all 4 detector elements.

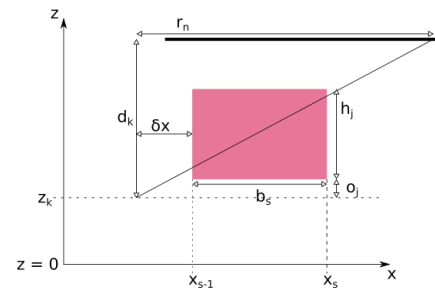
Since the sample is designed as consisting of cuboids with sharp edges, the path length are by design not differentiable (but mathematical continuous). Therefore the calculation of the respective thickness is divided in 4 possible cases (see Figure 5.6):

- LT: passing left and top edge (see a))
- LR: passing left and right edge (see b))
- BT: passing bottom and top edge (see c))
- BR: passing bottom and right edge (see d))

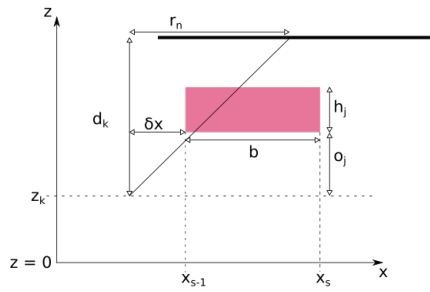
The path length of a beam through the layer j of the zone (s, p) is dependent on the (lateral) zone width b_s , the layer thickness h_j , the z-offset of this layer



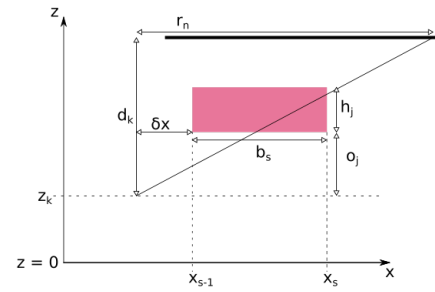
a) LT



b) LR



c) BT



d) BR

Figure 5.6: Possible cases in 2D: LT = left-top, LR = left-right, BR = bottom-right, BT = bottom-top.

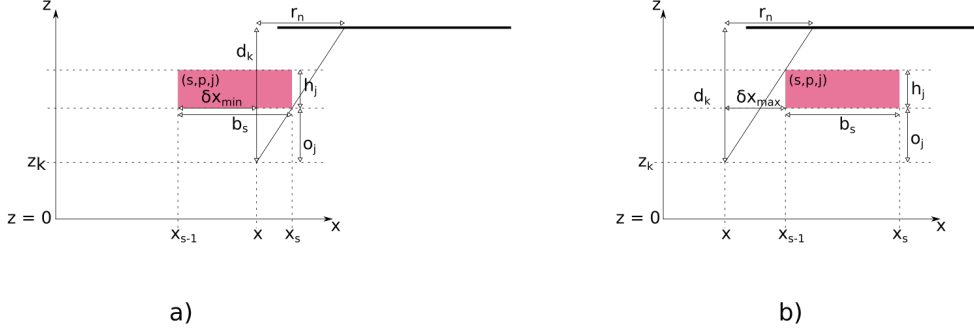


Figure 5.7: Illustration of the boundaries for $\delta x = x_{s-1} - x$. Note that in a) $\delta x < 0$

(relative to the z-scan point z_k)

$$o_j = \sum_{m=J_{s,p}}^j h_m - z_k \quad (5.7)$$

the angle $\alpha(r_n, d_k)$ of the respective beam and the distance δx of the current scan position (x, y) to the zone edge x_{s-1} . Depending on which edges the beam crosses, the path has to be calculated according to the upper case analysis.

First of all, the respective layer is only intersected by the beam, if

$$\delta x = x_{s-1} - x \quad (5.8)$$

$$\delta x \in [\delta x_{min}, \delta x_{max}] \quad (5.9)$$

$$(5.10)$$

Note that with increasing x (standard scan direction) δx is decreasing. If $x > x_{s-1}$ then $\delta x < 0$. Using the intercept theorem (see Figure 5.7) one gets the following intervall boundaries for δx :

$$\delta x < 0 \quad (5.11)$$

$$\frac{r_n}{d_k} = \frac{x_{s-1} + b_s - x}{o_j} = \frac{\delta x + b_s}{o_j} \quad (5.12)$$

$$\Rightarrow \delta x > \frac{r_n \cdot o_j}{d_k} - b_s = \delta x_{min} \quad (5.13)$$

$$(5.14)$$

(Note: Looking at Figure 5.7 one might get the impression that this case

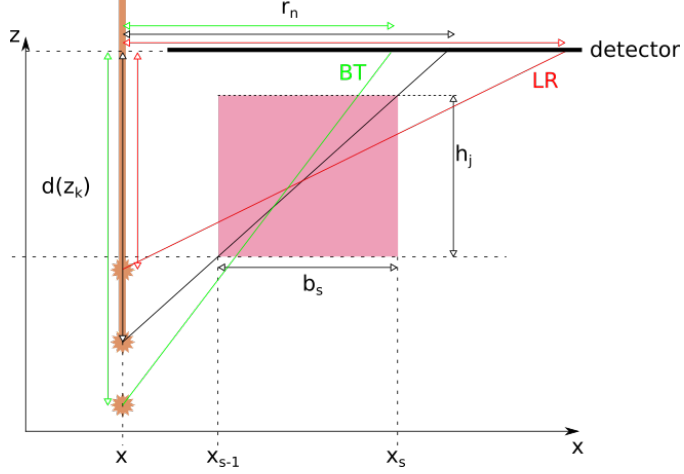


Figure 5.8: Illustration for the case analysis concerning BT and LR. For a certain beam characterized by $d(z_k)$ and r_n (assuming a 2D model) either the case BT or LR can occur for a certain layer j . Which case occurs depends on $\frac{h_j}{b_s}$. When the ratio $\frac{d_k}{r_n}$ is larger than $\frac{h_j}{b_s}$, the beam passes through bottom and top of the layer (green). If it's smaller it passes through the left and right edges (red).

can only occur when the scan point (zone (i, g)) is in the same zone (s, p) as the regarded layer j . This must not be the case. Similar situations e.g. may occur when an outer detector radius r_n is used.)

$$\frac{r_n}{d_k} = \frac{\delta x}{o_j + h_j} \quad (5.15)$$

$$\Rightarrow \delta x < \frac{r_n \cdot (h_j + o_j)}{d_k} = \delta x_{max} \quad (5.16)$$

$$(5.17)$$

If δx is not in this intervall, the path length l for the beam going to detector element (n, ϕ) is set to zero for this layer (s, p, j) and the beam origin (x, y, z_k) .

For a certain (x, y, z_k) position and detector radius r_n , the cases LR and BT cannot occure in the same layer, the respective condition is (see Figure 5.8):

$$h_j < \frac{b_s \cdot d_k}{r_n} : BT \quad (5.18)$$

$$h_j > \frac{b_s \cdot d_k}{r_n} : LR \quad (5.19)$$

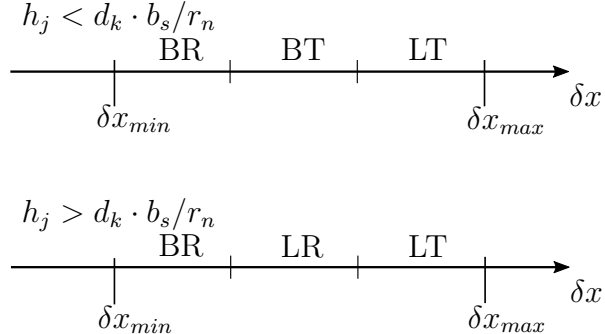


Figure 5.9: Illustration of the different cases for the calculation of the path length l of a beam traveling through a layer j in dependence of the relative position of the beam δx . The abbreviations indicate the edges of the layer zone which the beam cuts: BR = bottom-right, BT = bottom-top, LT = left-top, LR = left-right

This condition is based on a beam passing directly through the lower left and upper right corner (Figure 5.8, black beam).

For each of these two cases there are the 3 different possibilities (BR, LR/BT, LT), dependent on the current distance from the edge δx and the respective detector ring radius r_n (see Figure 5.9).

The calculation of l for the case $h_j < \frac{b_s \cdot d_k}{r_n}$ follows the equations:

$$\delta x < \frac{r_n \cdot (o_j + h_j)}{d_k} - b_s : \quad l_{BR} = \sqrt{\left(\frac{d_k}{r_n}\right)^2 + 1} \cdot \left(\delta x + b_s - \frac{o_j \cdot r_n}{d_k}\right) \quad (5.20)$$

$$\delta x \in [\frac{r_n \cdot (o_j + h_j)}{d_k} - b_s, \frac{r_n \cdot o_j}{d_k}] : \quad l_{BT} = \sqrt{\left(\frac{d_k}{r_n}\right)^2 + 1} \cdot \frac{r_n \cdot h_j}{d_k} \quad (5.21)$$

$$\delta x > \frac{r_n \cdot o_j}{d_k} : \quad l_{LT} = \sqrt{\left(\frac{d_k}{r_n}\right)^2 + 1} \cdot \left(\frac{(o_j + h_j) \cdot r_n}{d_k} - \delta x\right) \quad (5.22)$$

In case $h_j > \frac{b_s \cdot d_k}{r_n}$ the calculation of l_{BR} and l_{LT} are similar to (5.20) and (5.22), with different conditions towards δx :

$$\delta x < \frac{r_n \cdot o_j}{d_k} : l_{BR} \quad (5.23)$$

$$\delta x \in [\frac{r_n \cdot o_j}{d(z)}, \frac{r_n \cdot (o_j + h_j)}{d_k} - b_s] : l_{LR} = \sqrt{\left(\frac{d_k}{r_n}\right)^2 + 1 \cdot b_s} \quad (5.24)$$

$$\delta x > \frac{r_n \cdot (o_j + h_j)}{d_k} : l_{LT} \quad (5.25)$$

5.8 3D Considerations

In the previous section the calculation of the path length l was discussed only considering two spacial dimensions (side view, x and z).

Since the QUAD detector is annular, it detects radiation over (almost) the full 2π of the polar angle ϕ .

For a more accurate model, it is therefore necessary to consider the variation of the 'virtual' width of the layers when sliced along a vertical plane in ϕ (see Figure 5.10).

Moreover the distance $\delta\tilde{x}$ from the illumination point (x, y) in the zone (i, g) to the zone (s, p) needs to be projected on ϕ .

(Note: The following explanation is valid for the 1. angular quadrant ($0 < \phi < \frac{\pi}{2}$). The other quadrants can be dealt with analogously.)

Since either the zone border x_{s-1} or the zone border y_{p-1} define the distance to (x, y) , it is necessary to include a maximum condition:

$$\delta\tilde{x} = \max\left(\frac{x_{s-1} - x}{\cos(\phi)}, \frac{y_{p-1} - y}{\sin(\phi)}\right) \quad (5.26)$$

The following calculation of the beam path is formally identical to the calculation explained in the previous section with an appropriate change of the coordinate system and therefore will not be explained in detail. The simulation uses the same function for both, first calculating the projected width \tilde{b} of the zone (s, p) along the slice in ϕ and then uses this value for the determination of the actual path length l .

For example would the length of the green line segment in Figure 5.10 be needed to be used as \tilde{b} instead of the x-width b_s to calculate the actual path length l . In this case \tilde{b} would be calculated using equation (5.22), because it intersects zone (s, p) from left to top of the zone. The calculation of the projected lengths can be understood as using the same formula as for l but in a top view instead of a side view of the sample.

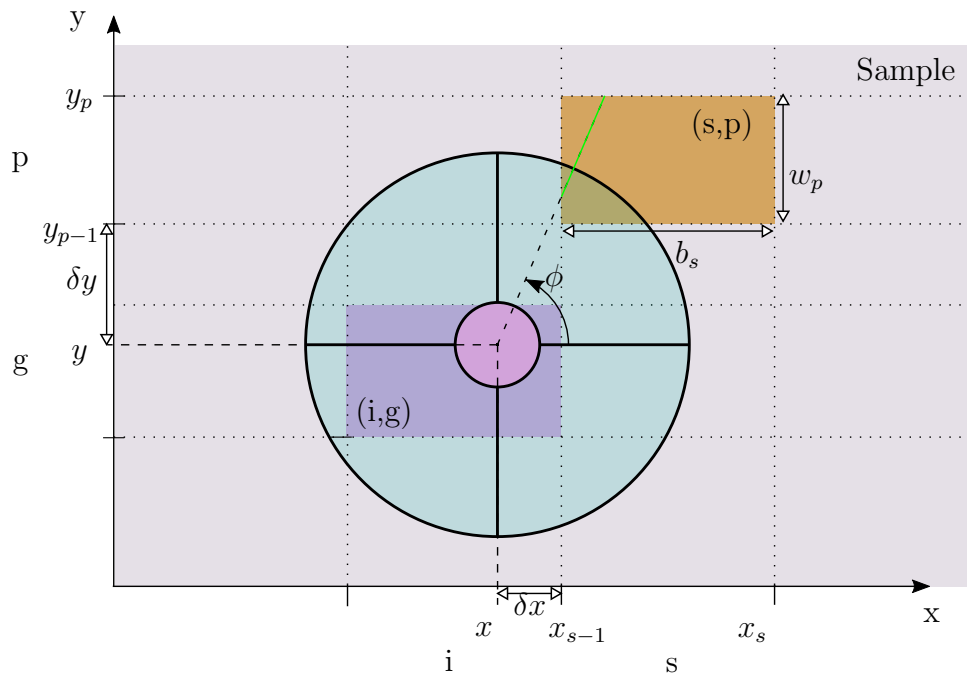


Figure 5.10: Top view of a model sample. The green line indicate the projected width of the zone (s, p) (orange) for the respective polar angle ϕ at the scan position (x, y) in zone (i, g) (violet). This width is dependent on the distances δx , δy , b_s , w_p and the angle ϕ . The radius r_n of the detector element is irrelevant at this point.

Chapter 6

Results

In the following chapter the first tests and results obtained with QUADaps are presented. They mainly focus on simple sample designs inspired by biological samples and are supposed to show the simulation capacities of QUADaps and evaluate the strength of the predicted absorption effects.

6.1 Stability Tests of the Algorithm and Error Estimation

Since QUADaps is designed to simulate effects for situations where the outcome of the experiment is not yet known and understood, it is worthwhile to first test the algorithms for simple cases, where the results are expectable. This is the objective of the following section.

In the case at hand, the first simple test would be the simulation of a line scan over a homogeneous sample with arbitrary lateral zone-borders. The crossing of a zone border shouldn't influence the calculated fluorescence signal in any way. The same has to be true for a homogeneous sample composed of layers of the same material. Both tests were combined in a sample illustrated in Figure 6.1.

The various scans summarized in Table 6.1 show that the mean intensity for the carbon fluorescence signal changes when the number of detector radii is changed. Here the intensity rises with the number of radii. This means the absorption path length is generally overestimated by the program for small numbers of radial zones N_r . This is understandable considering the used assumption that every virtual beam hits the respective detector element in the middle (see Section 5.5). Nevertheless, the deviation is small and the data indicates that the intensity approaches a constant maximum value for

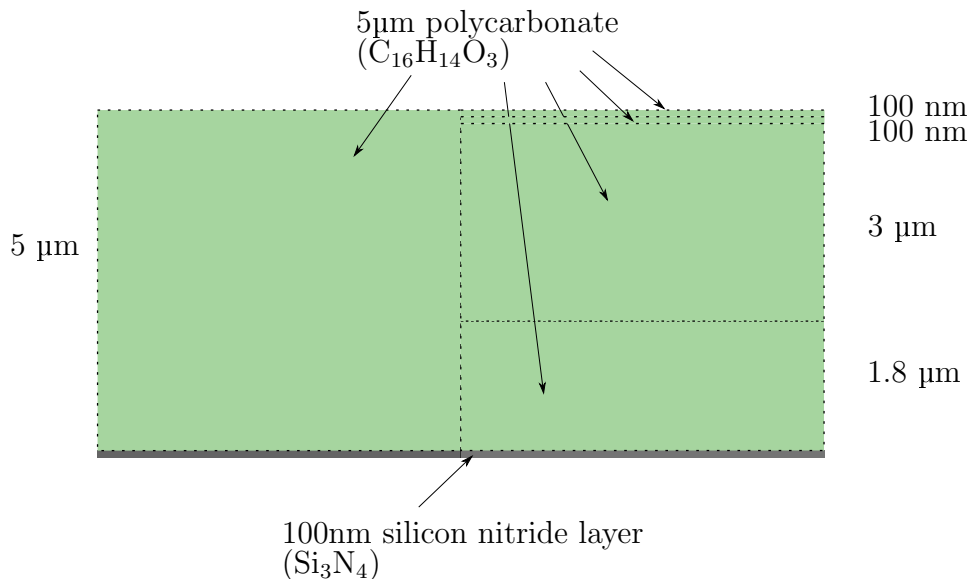


Figure 6.1: Illustration of a homogeneous sample made out of layered zones of the same material.

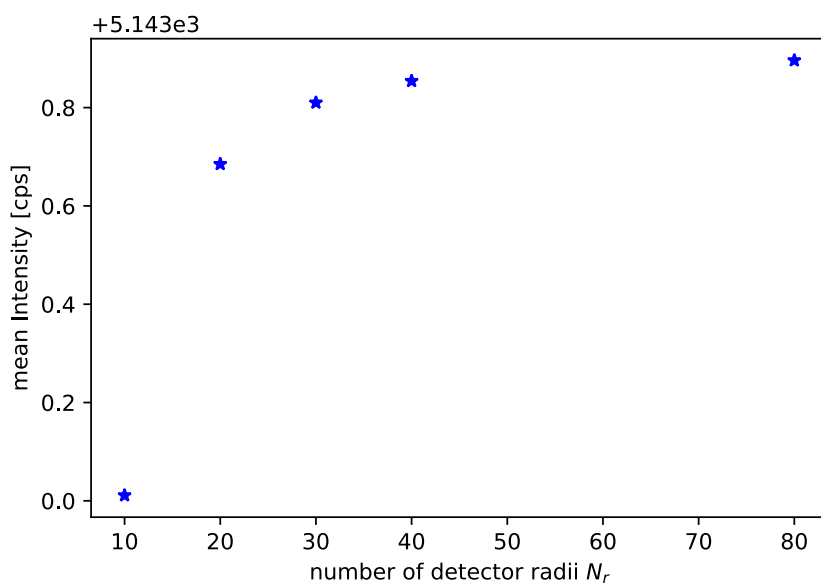


Figure 6.2: Mean carbon fluorescence intensity of a scan of a homogeneous sample (see Illustration 6.1) as a function of the simulated number of radial detector elements N_r .

Δz [nm]	Δx [μm]	N_ϕ	N_r	mean (carbon)	standard deviation
500	0.2	15	10	5143.023	1×10^{-2}
500	0.1	15	10	5143.025	1×10^{-2}
500	0.2	30	10	5143.027	1×10^{-2}
500	0.2	15	20	5143.702	1×10^{-2}
500	0.2	15	30	5143.827	1×10^{-2}
100	0.2	15	10	5143.011	1×10^{-12}
100	0.2	60	10	5143.011	4×10^{-12}
100	0.2	30	20	5143.685	5×10^{-12}
100	0.2	15	20	5143.685	3×10^{-12}
100	0.2	15	30	5143.810	1×10^{-12}
100	0.2	15	40	5143.854	3×10^{-12}
100	0.2	15	80	5143.896	1×10^{-12}
50	0.2	15	10	5143.001	2×10^{-12}
50	0.2	30	10	5143.001	1×10^{-12}
50	0.2	30	20	5143.676	4×10^{-12}
50	0.2	15	30	5143.800	1×10^{-12}
17	0.2	15	20	5143.668	6×10^{-6}

Table 6.1: Mean (summed) carbon fluorescence intensity and standard deviation for a line scan on a homogeneous sample defined in several zones (see Figure 6.1). The excitation energy was set to 0.7 eV.

$N_r \rightarrow \infty$ (see Figure 6.2). A sufficiently high number of radial intervals can thus be chosen to optimize integration time and accuracy.

The standard deviation of the intensity for a homogeneous sample should be as small as possible. Table 6.1 shows that the standard deviation is mainly dependent on the chosen step size Δz . This has two reasons: first, the step size should be smaller than the thinnest layer of the sample. Although the program accounts for 'incomplete' last steps when crossing a layer border, this is connected to a numerical error respectively a slight deviation on the overall thickness.

Second, if the stepsize is changed by the program due to an 'incomplete' step, as mentioned above, the exit angles and solid angle used for the calculation change a little bit, because they are dependent on the distance of the z-iteration point to the detector and thus on the step width. This behavior is inherent to the numerical integration used in QUADaps and rather shows the accuracy of the code than its instability.

The table moreover shows, that best accuracy is reached when the step size matches the layer thicknesses. Otherwise, similar to the case of too large steps, an additional numerical error is introduced.

Another test is changing the scan step width in x and y . It is to expect that a smaller step width will smoothen the signal for inhomogeneous samples. In a homogeneous sample this should have no effect, which was confirmed in by the scans summarized in Table 6.1.

6.2 Solid Angle and Working Distance

The theoretical solid angle curve following (4.1) suggests a maximum solid angle at a distance of about 1.42 mm between detector (metal frame) and sample surface. The position of this maximum is only dependent on the geometrical parameters of the detector (radii). Thus, it can be assumed to be the optimal distance for each measurement.

Since there is no encoded distance control implemented yet to measure this distance, it would be desirable to determine the actual working distance through the fluorescence detection itself. The change of the solid angle with distance could be used for this.

To test this strategy and validate the theoretical $\Omega(d)$ curve, a point measurement of a homogeneous reference sample at different distances d was carried out. The integrated fluorescence intensity (scaled with a proportionality factor and excluding scattering contributions) can be compared to the theoretical curve and the curve the manufacturer Bruker provided.

Since the absolute distance was unknown, a constant offset d_0 was included

in the fit. Moreover the effective detector radii are themselves dependent on the distance to the sample, because the chip is positioned a little underneath the metal holder frame (see Section 4.1). The metal frame is in the following considered to define the detector surface. The projection of the frame radii on the silicon chip active area are included in the fit function. The fit function thus had the form:

$$\begin{aligned} I(d) &= A \cdot \Omega(d) + B \\ &= A \cdot 2\pi(1 - f_s) \left(\frac{r_a(d)^2 + (d + d_0)^2 - (d + d_0)\sqrt{r_a(d)^2 + (d + d_0)^2}}{r_a(d)^2 + (d + d_0)^2} \right. \\ &\quad \left. - \frac{r_i(d)^2 + (d + d_0)^2 - (d + d_0)\sqrt{r_i(d)^2 + (d + d_0)^2}}{r_i(d)^2 + (d + d_0)^2} \right) + B \end{aligned} \quad (6.1)$$

The projection functions are:

$$r_i(d) = \frac{d + d_{Si}}{d + d_{uE}} \cdot r_{i,nominell} \quad (6.2)$$

$$r_a(d) = \frac{d + d_{Si}}{d + d_{lE}} \cdot r_{a,nominell} \quad (6.3)$$

The relative change in distance was achieved by the mechanical manipulators of the detector mounting. The accuracy was estimated to about $\pm 10 \mu\text{m}$. In the fit radii were fixed and only the unknown distance offset d_0 and the proportionality factor A were adjusted. Figure 6.3 (assuming $B = 0$) shows that the fit model without a constant offset is well suited to represent the data. At large distances the fit is showing a larger deviation from the measurement data. A similar behavior is visible at comparable measurements of the detector manufacturer Bruker (see [6]). The uncertainty of the measurement data is expected to be higher in this regime, because less intensity reaches the detector.

A fit including an additional constant intensity offset B is even better matching the data points (see Figure 6.4). This additional offset could be understood as a constant background signal, due to noise or even independent of the sample and detector. Since this is unlikely for the setup and detector type, this approach would need to be verified in future measurements.

Since the actual measurements are supposedly performed at a distance close to the optimal distance, it is experimentally most important to have the possibility to describe the solid angle curve in this region, which the presented measurement and fit confirm.

From an experimental perspective it is important to note, that the maximum

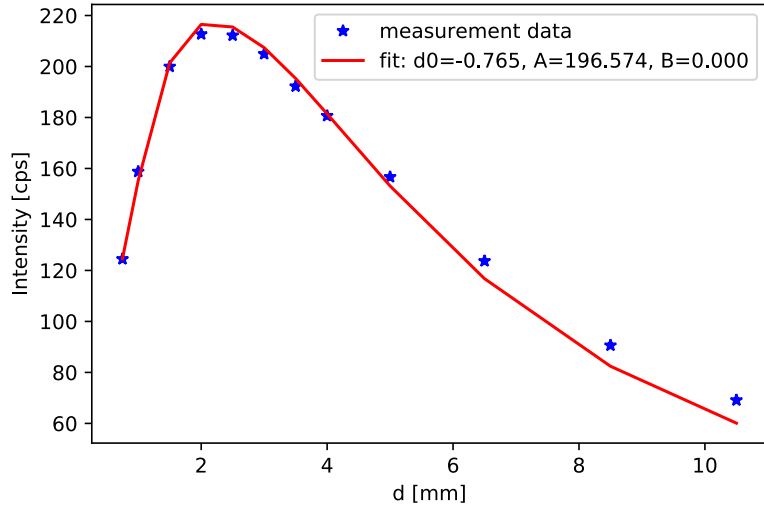


Figure 6.3: Measured intensity sum in the energy range 0.253-1.341 keV as a function of the distance d between sample and detector. Excitation energy was 1.5 keV. The fit follows (6.2) with free parameters d_0 and A .

of the curve is rather broad (see also Section 4.1). This is on the one hand positive, since it poses less restrictions on the optimal positioning of the detector relative to the sample and the flatness of the sample surface itself.

On the other hand it means, that measuring the actual distance with this method leaves room for a relative large uncertainty, if only positions close to the optimum position are used for the fit.

To position the detector correctly without additional direct distance measurements or encoding, a scan of the intensity as a function of the distance and a fast fit could nevertheless be suggested.

6.3 Simulation Results

The QUADaps simulation program described in Section 4.1 is meant as a tool to better understand the effects a large solid angle of detection can have on fluorescence measurements. It is specifically designed for the detector and setup of the AnImaX end station (see Section 3.5). It is a sole forward calculation tool and therefore not meant for direct data evaluation, but rather for comparison of measurement data with a theoretical model. Furthermore it can be used to pre-evaluate possible samples and measurement strategies beforehand and give an impression of which effects have to be expected. On

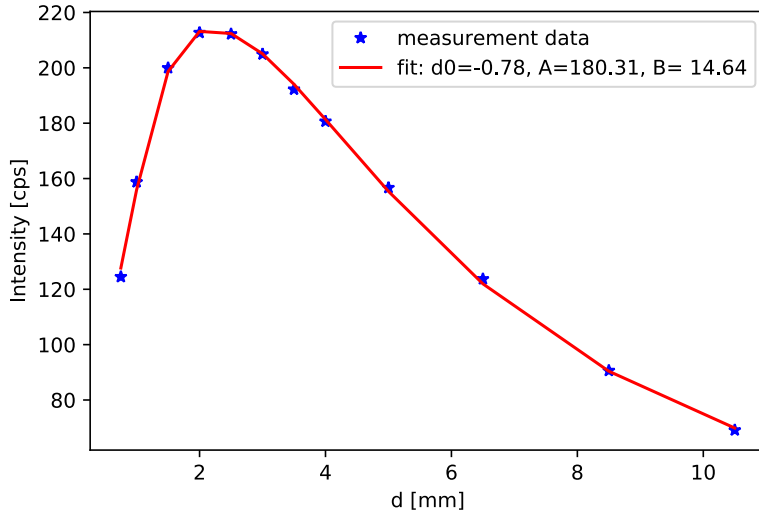


Figure 6.4: Measured intensity sum in the energy range 0.253-1.341 keV as a function of the distance d between sample and detector. Excitation energy was 1.5 keV. The fit follows (6.2) with an additional constant intensity offset B . The free fit parameters were d_0 , A and B .

the long run, it is meant as a first step towards a quantitative evaluation of fluorescence imaging data, which takes inhomogeneous effects into account. The special feature of 4 independent detector cells is here expected to give valuable additional information concerning 3D features as surface structures and buried inhomogeneities.

In the following, the program was exemplary used to study a number of samples which were expected to show different effects.

Starting with homogeneous samples and the comparison to already existing approaches for large solid angle detection the simulated samples were all designed to resemble possible real samples. Therefore a light, organic matrix on a thin Si_3Ni_4 window (as used in the setup) was chosen. The simulations explore the influence of varying structure size, composition, position (depth) and density. The motivation is twofold: finding lower limits of detection, looking for characteristic features in the signal that can be used as a indicator for a certain property and finally suggesting possible model sample layouts, that could be measured with AnImaX.

6.3.1 Homogeneous Samples - Comparison to Equivalent Angles

It was suggested by Malzer et al. [13] (see Section 3.2) to use an equivalent angle approach to allow for non-parallel excitation and observation beams for homogeneous samples.

To determine the equivalent angle for a certain setup, they used Monte Carlo simulations. Besides finding a much lower error when using the equivalent angles for incident and detected beam instead of the nominative geometrical angles, they also showed that the equivalent angle is rather independent to the sample composition and excitation energy, as long as no absorption edges of the main components occur between the excitation and detected energy. In the following the examples for equivalent angles of certain setups Malzer et. al. published shall be compared to the simulation with QUADaps.

Since QUADaps was designed for a specific experimental setup, only a limited variety of cases can be simulated. The main restriction is a parallel narrow beam assumption for the incoming radiation. Therefore only one of the three examples given in [13] was possible to simulate. The specifications are given in the publication by Malzer et. al. [13] in Table 2, example 2 (transferred to the coordinate system used in the rest of this thesis):

The incident beam has a $\theta = 45^\circ$ inclination to the sample surface and no beam divergence. The observation angle is $\Phi = 90^\circ$ and a beam divergence of $\alpha = 30^\circ$ is assumed. The equivalent observation angle determined by Monte Carlo simulations was given as $\Phi_{eq,MC} = 79.4^\circ$, deviating about 10.6° from the nominal observation angle.

To simulate a similar situation with the QUADaps program, the inner detector radius was set to $r_i = 0$ mm and the outer $r_a = 0.66$ mm, which equals circular detector with a full opening angle of $\alpha = 30^\circ$ on a sample-detector distance of $d = 2.5$ mm.

To determine an equivalent angle, the xrfLibrary itself was used directly to calculate the primary fluorescence intensity at different observation angles Φ assuming a constant solid angle based on the above given parameters. Parallel the fluorescence intensity for the nominal observation angle of 90° is calculated with QUADaps. The angle where the traditional calculation and the QUADaps program yield the same result can be considered as comparable to the equivalent angle, introduced by Malzer et al.

Malzer et al. studied the relative deviation of the intensities calculated with the equivalent angle from intensities obtained with full Monte Carlo simulations for a range of parameters $\mu\rho D$ and $k = \frac{\mu_i}{\mu_i + \mu_0}$ (where $\mu = \mu_0 + \mu_i$ is the effective mass absorption coefficient for excitation and fluorescence energy,

ρ the density and D the sample thickness). This accounts for a wide range of possible sample compositions and energies, although it does not consider absorption edge effects.

QUADaps was not designed to make this kind of systematic studies possible, but rather for simulating specific sample compositions and layouts. Therefore the results can only be compared on an exemplary level.

In Table 6.2 the equivalent angles for a carbon, sodium and iron sample each with a thickness of $10\text{ }\mu\text{m}$ (C, Na) and $0.5\text{ }\mu\text{m}$ (Fe) for different excitation energies are listed. The thickness was chosen so that the assumption $\mu\rho D \in [0, 6]$ was fulfilled. The effective mass absorption coefficient μ was calculated using the sum of the absorption coefficient of the incoming radiation and the fluorescence lines which were excited by the incoming radiation. Note that the calculations sum over all excited K, L and M lines.

The equivalent angles calculated with QUADaps are in a similar magnitude as published in [13] but deviate depending on the used energy (and thus the energy dependent absorption coefficient μ). The angles becomes steeper with rising energy. Running simulations with heavy elements and/or large thicknesses, such that $\mu\rho D$ exceeded the range studied by Malzer ($\mu\rho D \in [0, 6]$) showed that the resulting equivalent angles differ strongly from Malzer's results. The same is true for very light and thin samples.

This behavior is most likely due to the negligence of absorption edges in the Monte Carlo simulations. Moreover the QUADaps simulations include a changing solid angle of detection (or divergence angle) depending on the z-iteration, which most likely is not included in the Monte Carlo simulations. Since the solid angle has a strong influence on the calculated intensity, it is plausible that the equivalent angle obtained by comparing the intensities of the classical FP calculation (with a fixed solid angle) and the QUADaps simulation, is also dependent on slight changes of the used solid angle.

Considering the fundamental differences in the compared approaches, the shown agreement can thus be considered as a first validation of the QUADaps calculations.

6.3.2 Homogeneous Samples - Surface Structures

To illustrate the capacities of QUADaps and give a first example of the expected effects caused by the QUAD geometry a homogeneous sample with a simple surface structure was simulated (see Figure 6.5).

The sample consists of a $500\times 500\times 500\text{ nm}$ (XxYxZ) polycarbonate cuboid on a $5\text{ }\mu\text{m}$ thick polycarbonate matrix on a 100 nm silicon nitride window.

Figure 6.6 shows a line scan in x direction over the y-center of the cuboid. Since at this y position the cuboid is symmetrical in y-direction the two de-

Z (material)	E_0 [keV]	D [μm]	ρ [$\frac{\text{g}}{\text{cm}^3}$]	Δz [μm]	$\mu\rho D$	α [$^\circ$]
6 (C)	1	10	2.20	0.1	9.19	81.52
6 (C)	2	10	2.20	0.1	4.98	82.20
6 (C)	3	10	2.20	0.1	4.52	82.27
6 (C)	4	10	2.20	0.1	4.39	82.29
11 (Na)	2	10	0.97	0.1	2.05	78.10
11 (Na)	3	10	0.97	0.1	1.03	78.55
11 (Na)	4	10	0.97	0.1	0.76	78.66
26 (Fe)	1	0.5	7.87	0.1	4.39	77.45
26 (Fe)	3	0.5	7.87	0.1	1.06	80.17
26 (Fe)	7	0.5	7.87	0.1	0.87	80.29
26 (Fe)	7.2	0.5	7.87	0.1	1.03	80.42
26 (Fe)	8	0.5	7.87	0.1	0.99	80.42

Table 6.2: Equivalent angles α for exemplary samples for a setup comparable to example 2 in [13].

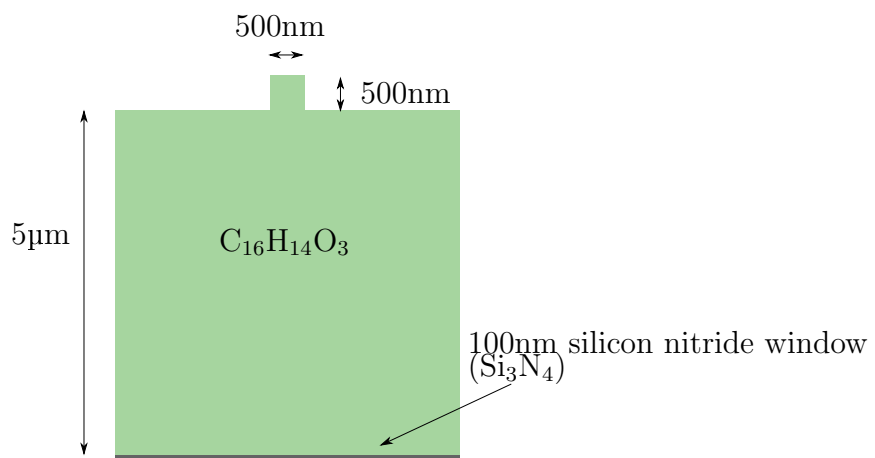


Figure 6.5: Illustration of a homogeneous sample with a surface structure. Side view, the default scan direction for a line scan is from left to right.

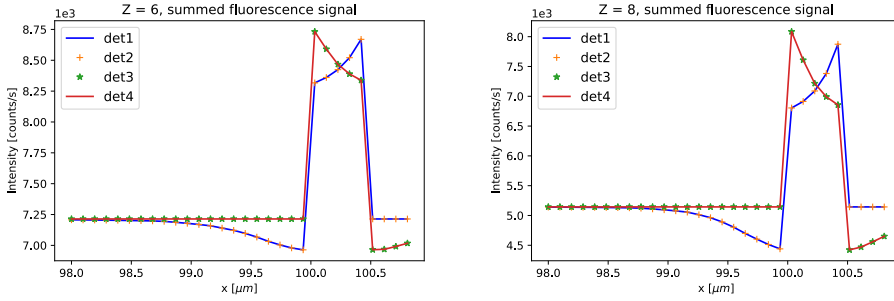


Figure 6.6: Simulation of a line scan over the sample illustrated in Figure 6.5, at the y-center of the surface structure. Simulation parameter: excitation energy $E_0 = 0.7 \text{ keV}$, z-step width $\Delta z = 100 \text{ nm}$.

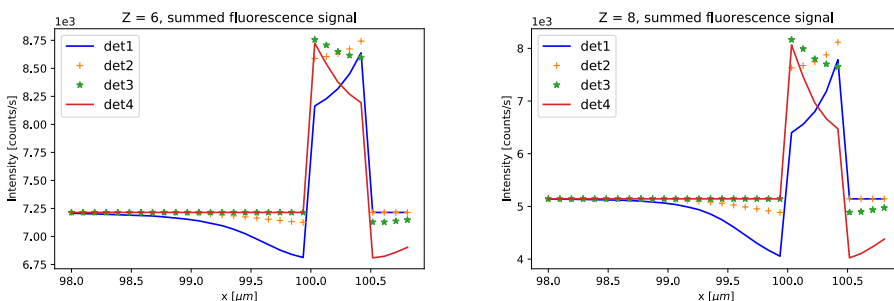


Figure 6.7: Simulation of a line scan over the sample illustrated in Figure 6.5, a little offset to the center of the surface structure. Simulation parameter: excitation energy $E_0 = 0.7 \text{ keV}$, z-step width $\Delta z = 100 \text{ nm}$.

tector cells in positive x-direction (det1 and det2) show the same signal. The same is true for the two detector cells in negative x-direction (det3 and det4). For $98.7 \mu\text{m} < x < 100 \mu\text{m}$, detector cell 1 and 2 both show the increasing absorption of the primary fluorescence signal ('shadow') due to the surface structure, when detector cell 3 and 4 still show the signal of the unstructured surrounding. When the excitation beam (scan point) hits the surface structure ($100 \mu\text{m} < x < 100.5 \mu\text{m}$) the overall signal increases. The left hand side detectors (det3 and det4) show a higher signal because the radiation generated in the upper layers of the sample, close to the cuboids edge, experiences almost no attenuation. In the following, this effect is going to be referred to as 'edge enhancement'. The signal shows the same effects on the other side of the surface structure for the respective detector cells. The sight deviation of the peak heights of the two detector pairs is due to the x-step discretization and would be reduced if a finer step width in x would be chosen.

Figure 6.7 shows a similar scan at a different y position, where the structure is not symmetrical in y, to illustrate that QUADaps indeed accounts for the 3-dimensional shape of the defined sample.

6.3.3 Inhomogeneous Samples - Information Depth

Scanning microscopy per se is not sensitive to 3-dimensional structures, the generated image is always a projection onto a plane. Therefore it is not necessarily well defined from which depth in the sample the detected information is coming. This becomes problematic in thick samples which are not homogeneous in depth.

Therefore it would be valuable if the additional information generated by the 4 detection directions of the QUAD detector could be used to judge if a visible structure is at the surface or buried in the sample.

As a simple model system a cubic iron particle of side length 100 nm is simulated at different depth in a polycarbonate matrix (see Figure 6.8). The excitation energy was set to 0.7 keV and the incoming intensity to 1×10^9 cps. Figure 6.9 and 6.10 show the effects the different depth of the particle has on the signal for different excitation energies below (700 eV) and above (800 eV) the absorption L_{2,3}-edges of iron. The core of these simulations was to estimate the influence of the particle absorption rather than its fluorescence, which would be more pronounced at higher excitation energies.

First of all it is to note that the overall sample thickness at the position of the particle for the sample with a particle on the surface (orange line) is 100 nm larger than for the other simulations, because the polycarbonate is thicker. This explains why the carbon signal in this case is higher at the position of the particle than for the case of a particle in the surface (green

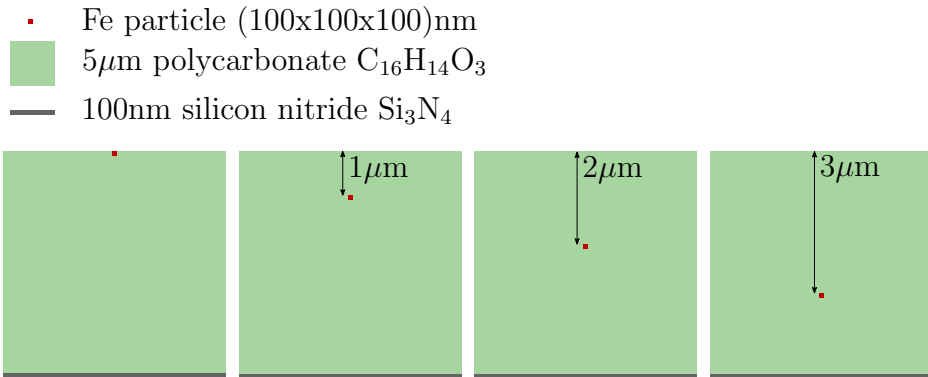


Figure 6.8: Illustration of iron particles (red) in different depths in a polycarbonate matrix (green) on a Si_3N_4 window (grey), side view.

line). The elevated structure when the particle is on the surface leads also to a different shape of the shadow. If similar effects could be shown to be resolvable in actual experiments, they probably could be used to indicate surface and bulk structures. A similar approach is thinkable to help identify thickness variations in contrast to density variations.

Looking at the particle in varying depths, it becomes clear that the form of the shadow generally stays the same, but the absolute height of the intensity drop depends strongly on the depth of the structure, as can be expected. In this special case, an iron particle of the given size would not be resolved anymore if it is deeper than approximately $2\mu\text{m}$ below the surface. This is an important information for the sample preparation, e.g. when deciding how thick a biological tissue sample stained with iron nano particles should maximally be to still be examined with 700-800 eV.

Additionally several particles on top of each other are simulated (see Figure 6.11), to see if they could be resolved individually. The simulations depicted in Figure 6.12 and 6.13 indicate that the signal is mainly influenced by the depth of the particle closest to the surface. Additional particles positioned directly underneath, change the signal only insignificantly. For this specific sample class, this means that even the QUAD detector would not be able to distinguish between this kind of nano particle accumulation under this excitation energy.

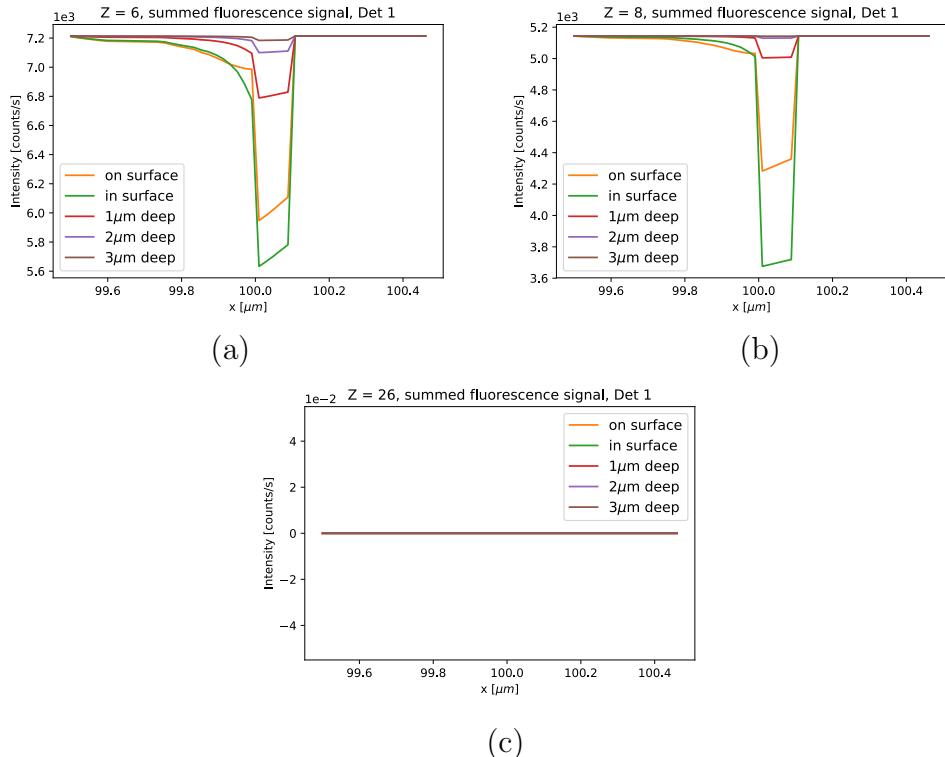


Figure 6.9: Fluorescence signal in detector 1 for an iron particle buried in different depth in a polycarbonate layer (see Figure 6.8):

(a) carbon ($Z = 6$), (b) oxygen ($Z = 8$), (c) iron ($Z = 26$).

The excitation energy was 700 eV (below the iron L_{2,3}-edges). Note the change in the shape of the shadow between the particle on the surface and in the surface. The signal does not change significantly when the particle is lower than 2 μm underneath the surface.

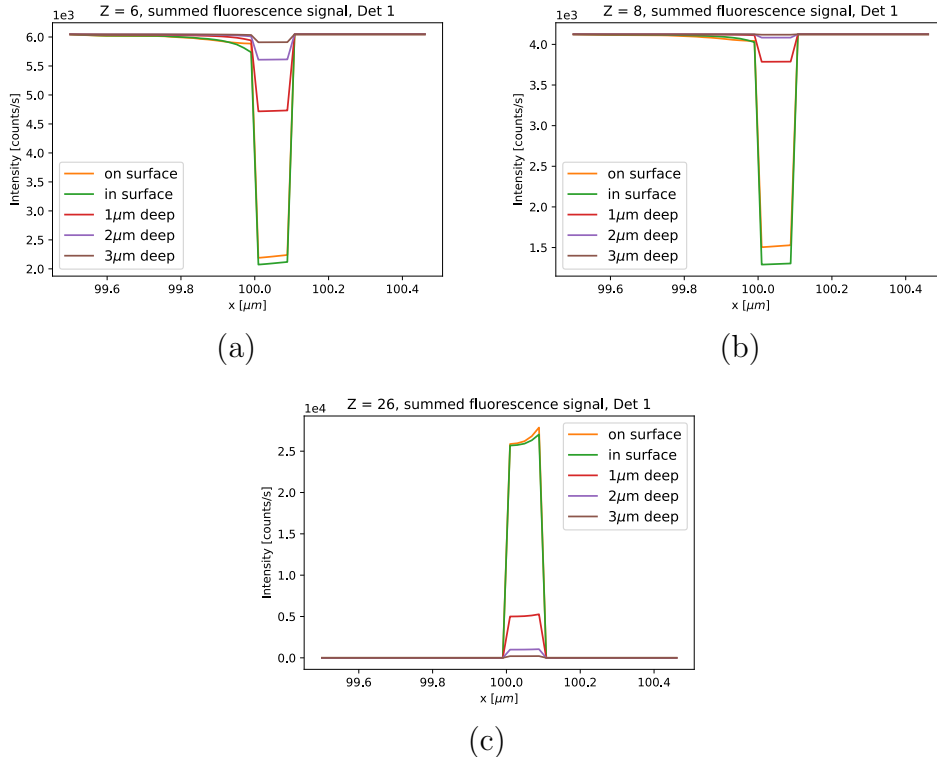


Figure 6.10: Fluorescence signal in detector 1 for an iron particle buried in different depth in a polycarbonate layer (see Figure 6.8):

(a) carbon ($Z = 6$), (b) oxygen ($Z = 8$), (c) iron ($Z = 26$).

The excitation energy was 800 eV (above the iron $L_{2,3}$ -edges). Now the iron L-lines are excited and show a decreasing iron signal dependent on the depth of the particle.

- Fe particle (100x100x100)nm
- 5 μ m polycarbonate C₁₆H₁₄O₃
- 100nm silicon nitride Si₃N₄

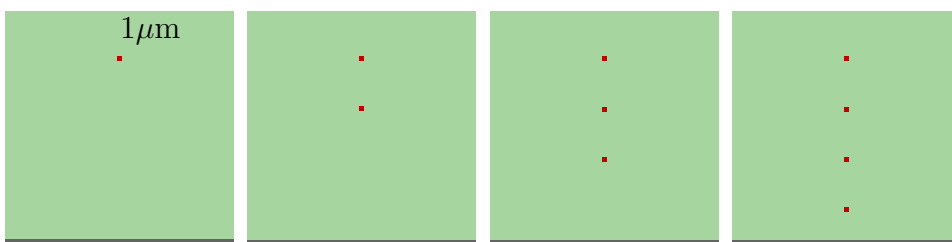


Figure 6.11: Illustration of iron particles (red) in different depths in a polycarbonate matrix (green) on a Si₃N₄ window (grey), side view.

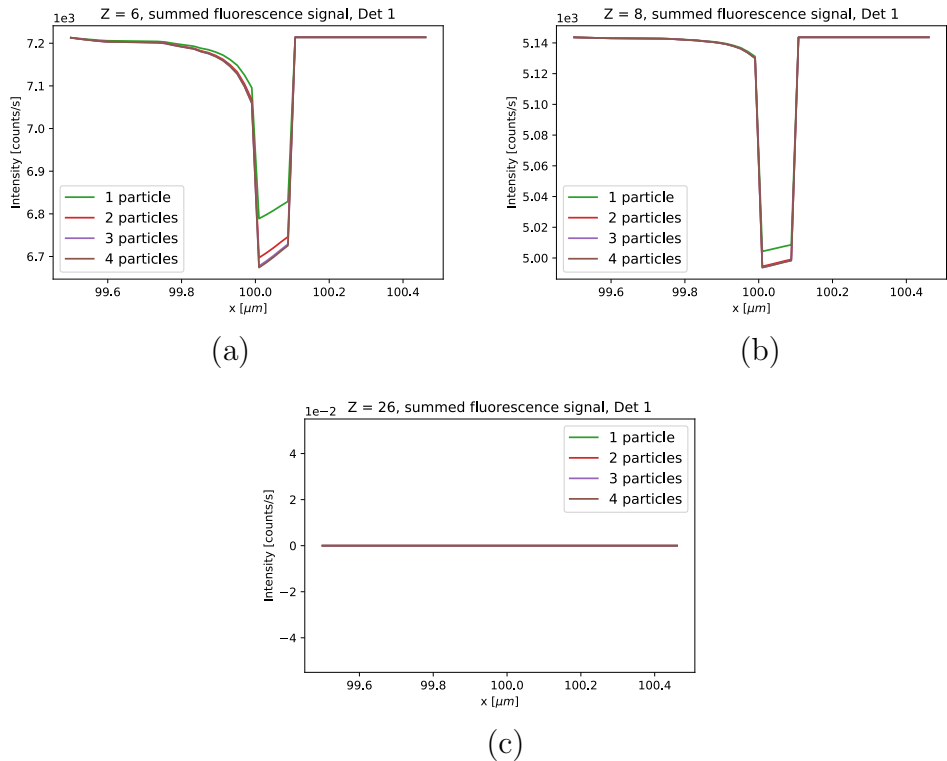


Figure 6.12: Fluorescence signal in detector 1 for several iron particles buried in a polycarbonate layer (see Figure 6.11):

(a) carbon ($Z = 6$), (b) oxygen ($Z = 8$), (c) iron ($Z = 26$).

The excitation energy was 700 eV (below the iron L_{2,3}-edges). The signal does not change significantly when more than two particles are located underneath each other at the same (x, y) position.

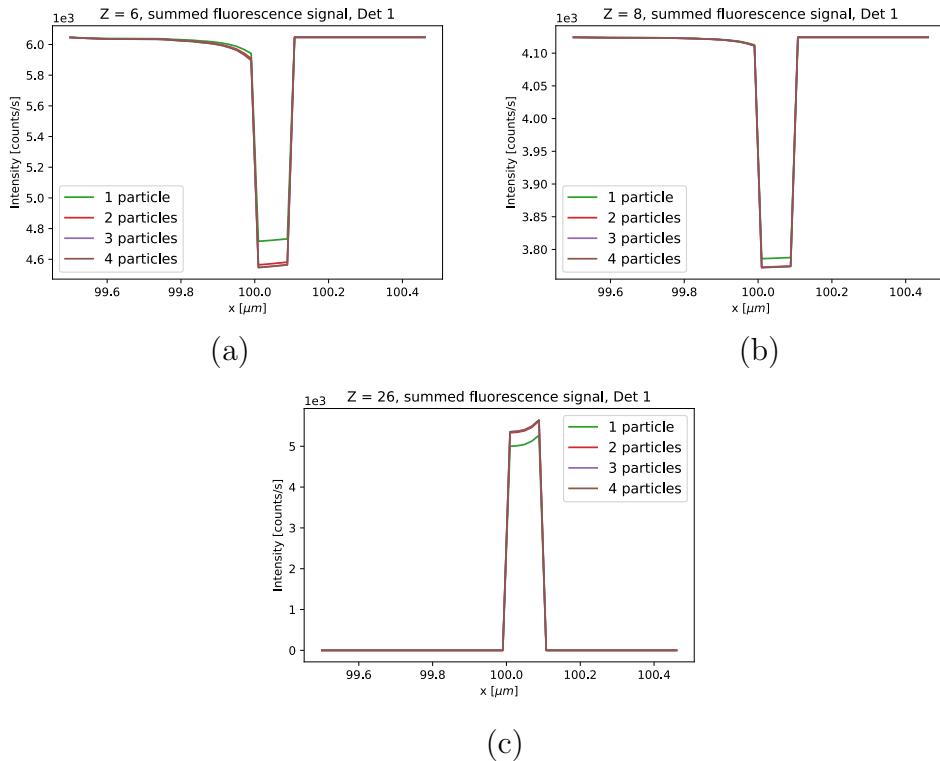


Figure 6.13: Fluorescence signal in detector 1 for several iron particles buried in a polycarbonate layer (see Figure 6.11):

(a) carbon ($Z = 6$), (b) oxygen ($Z = 8$), (c) iron ($Z = 26$).

The excitation energy was 800 eV (above the iron L_{2,3}-edges). The iron fluorescence signal at this excitation energy is mostly independent of the number of particles, due to the matrix absorption.

6.3.4 Inhomogeneous Samples - Area Mapping

To illustrate the possibility of full area mapping with QUADaps, a sample with a more complicated structure was chosen. The simulated area map is meant to simulate fluorescence maps possible with the AnImaX end station. The simulated sample consists of a 3 μm thick polycarbonate matrix in which two iron cuboids of 5x5x1 μm side length are embedded. The iron cuboids overlap at one edge and have a horizontal distance of 1 μm , see Illustration 6.14.

To properly excite the iron and reduce absorption of the matrix an excitation energy of 3 keV was simulated. For an acceptable simulation time the simulation parameters were chose rather coarse: step width $\Delta z = 0.2 \mu\text{m}$, $N_r = 20$ and $N_\phi = 15$.

The x and y step size was 0.33 μm and a full area of 17 $\mu\text{m} \times 17 \mu\text{m}$ was scanned.

The resulting elemental area maps are depicted in Figure 6.15 to 6.18. The left side of the figures show the signal in each individual detector cell, the larger map at the right side show the sum signal of all four detector cells.

The recording of the sum signal would be the natural first approach when measuring a sample. The electronic signal analysis in the QUAD detector makes it impossible to distinguish between the individual cells, when all of them are used for the measurement. If the signal in different detectors are to be compared, they need to be measured individually (by repeating the same scan several times). The simulation is not restricted in this way, since each detector cell is implemented separately.

The comparison between the signals show the predicted shadow and edge enhancement effects. How strongly these effects are pronounced depends on the element and excitation energy.

The traditional approach in a fluorescence microscopy measurement would be to determine the position of the iron particles by looking solely at the iron signal. Figure 6.18 shows the iron signal. Particle A yields an intense iron fluorescence signal and even shows edge enhancement at its lower and left edges, because the iron fluorescence radiation is less strongly absorbed by the polycarbonate matrix enclosing it than by the particle itself. Particle B is only excited by a fraction of the incoming radiation due to the absorption of the polycarbonate above it. Combined with the stronger absorption on the way out of the detector, the iron fluorescence intensity is only about a sixth of the intensity coming from particle A. Not knowing the z-position of the particles, this could be easily interpreted as a lower particle thickness or density/iron concentration.

A first hint that this is not the case can be seen in the silicon map (Figure

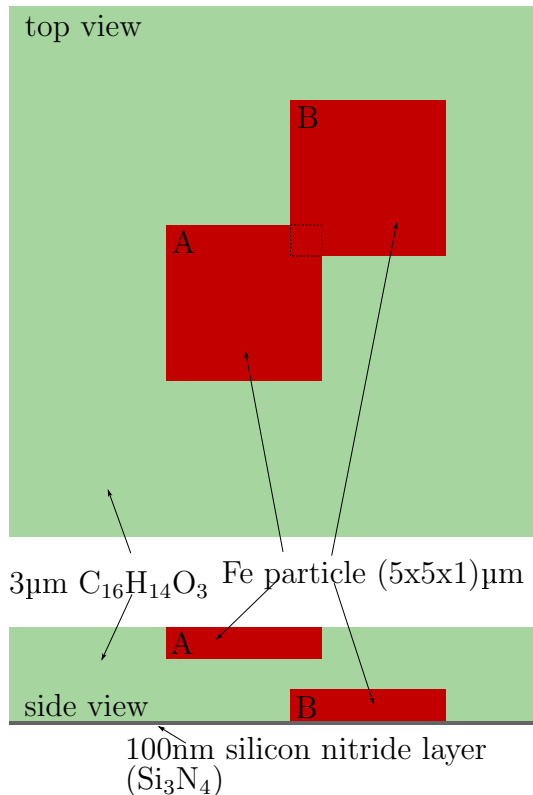


Figure 6.14: Illustration of iron particles (red) in different depths in a polycarbonate matrix (green) on a Si_3N_4 window (grey), top view and side view.

6.17). The silicon signal solely comes from the Si_3N_4 support window on the backside of the sample, which is homogeneous all over the sample area. In the sum signal map strong shadow or blurring effects can be seen especially around particle A. The different shapes of the absorption shadows created by particle A and B indicate the z position of these particles. The wider the shadow is spread and a flatter signal gradient indicate a particle closer to the detector, because the radiation coming from the backside of the sample (silicon nitride window) originating from lateral positions beside the particle has to pass the upper particle even at a larger lateral distance to it, than the lower particle, which is only passed if the radiation was generated close to its borders.

Another indication of the z-position of the particles are the carbon and oxygen signal, which both are stronger at the position of particle B, because the layer above the particle generates fluorescence, whereas particle A absorbs most of the incoming and fluorescence radiation before it reaches the polycarbonate.

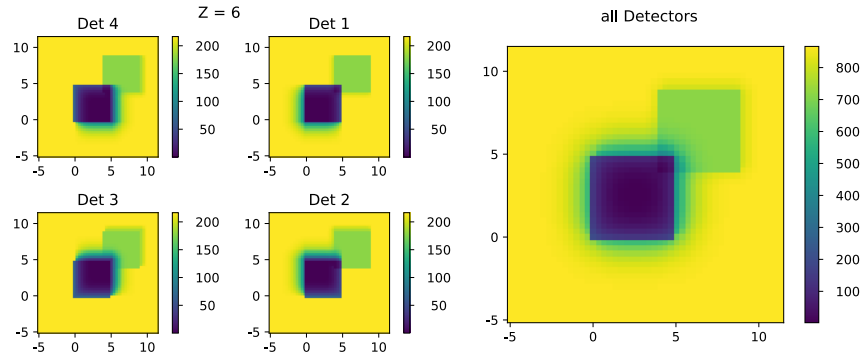


Figure 6.15: Carbon ($Z = 6$) map of the sample illustrated in Figure 6.14, excitation energy $E_0 = 3$ keV.

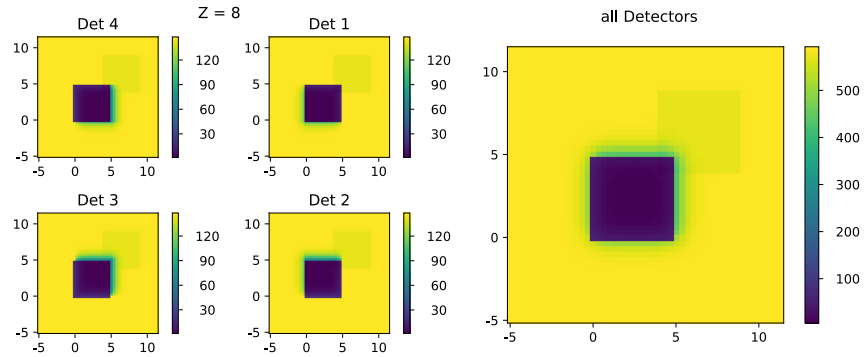


Figure 6.16: Oxygen ($Z = 8$) map of the sample illustrated in Figure 6.14, excitation energy $E_0 = 3$ keV.

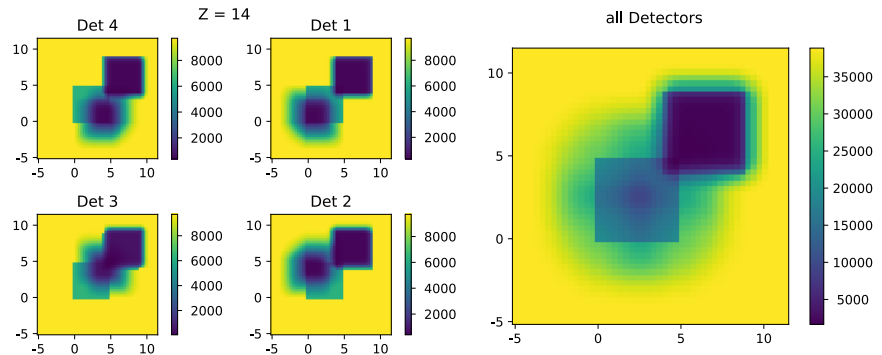


Figure 6.17: Silicon ($Z = 14$) map of the sample illustrated in Figure 6.14, excitation energy $E_0 = 3$ keV.

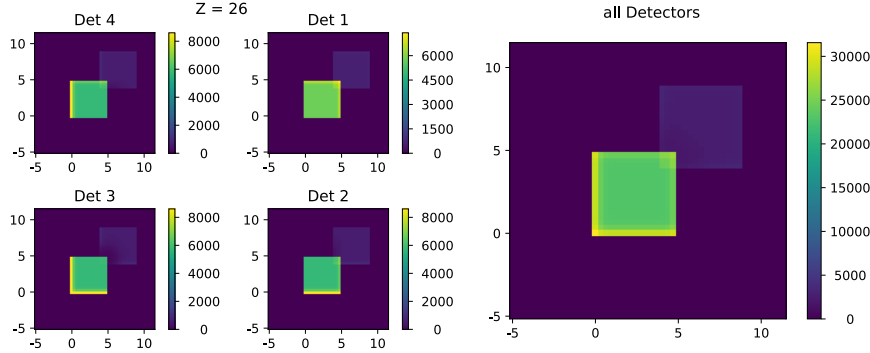


Figure 6.18: Iron ($Z = 26$) map of the sample illustrated in Figure 6.14, excitation energy $E_0 = 3\text{ keV}$.

6.4 Comparison to Experimental Results

Computer simulations can only serve as a tool to understand the actual experiment better. The included assumptions and simplifications might appear sensible enough but only the comparison with experimental data can indicate the correctness of the used model.

As a first test a sample was prepared which was expected to show strong shadowing effects due to its geometrical structure and did not need a sophisticated manufacturing process.

The measured sample comprised of a 100 nm thick silicon nitride window on which a stainless steel disc (1.4401) of 1 mm diameter and 50 μm thickness was glued with transparent nail polish (see Figure 6.19). The measurement was conducted at the PTB PGM beamline at BESSY II (Berlin, Germany), at a photon energy of 1500 eV.

The scan was performed as a 100x5 μm scan with a 1 μm step size. Each point was measured for 4 s to have a sufficient high signal.

The data evaluation concentrated on the nitrogen in the Si_3N_4 substrate window, since the excitation energy of 1.5 keV lies below the Si K-edge and thus does not excite the Si atoms. To account for background and possible peak overlap, the fluorescence intensities were deconvoluted using the PyMCA batch fitting function. The resulting intensities are given in netto peak area. The fit included the following elements: C (nail polish), N (silicon nitride window), O (nail polish + oxidation), Ca and Cr (steel). Calcium was included although it was not expected to be part of the sample, because it greatly improved the fit. Calcium could have been easily introduced by the sample preparation.

Since the scan was performed close to the y-center of the disc, the curvature

is large compared to the y-scan width. Therefore it is justified to assume a straight edge instead of a curved and sum over the 5 scan lines for a better statistic. That this assumption holds was also verified by looking at the position of the edge in each line singularly. They are in good agreement with each other.

Based on the nominal experimental and sample parameters as start values, the measured line scans were simulated. Since the thickness of the nail polish layer was unknown, several thicknesses between 0 μm -10 μm were simulated and compared to the data.

Moreover, the simulation is restricted to pixelated shapes. Therefore an approximation of the circular form of the steel structure was necessary. Several simulations were performed using different pixel grids ranging from assuming a simple square up to a 25x25 px/mm² grid.

Since it was impossible to register the exact scan position in the experiment, different y positions were simulated, the best matching simulation is depicted in Figure 6.20. The simulation and measurement do not match perfectly, especially the gradient of the shadow is not simulated properly. This can have various reasons, originating in the structure and limitations of the simulation program. Since only rectangular shapes can be defined, it is not possible to model the circular shape of the steel disc perfectly. In the shown simulation a decomposition into 25x25 px was used. During the simulation process it became apparent, that finer decomposition resulted in better matching. For actual samples it therefore pays off to use fine grids for non-rectangular shapes. Moreover, as the microscopy image in Figure 6.19 shows, the sample was contaminated with nail polish during the sample preparation. This was only roughly included into the simulation, because the thickness of the layer is unknown. Furthermore it is very likely that the edge of the steel disc was rough in the micrometer range, since it was not manufactured to meet standards in this respect. Another possible origin of the deviation is the limitation of QUADaps to parallel positioning of detector and sample surface. Since the steel is a comparably high structure on the silicon nitride window, even a slight tilt of the sample plane would result in a non perpendicular geometry, which cannot be simulated accurately with QUADaps.

Nevertheless, this example shows that the predicted shadow effects actually occur in fluorescence microscopy imaging, if the sample is inhomogeneous or structured. The effect is very well visible using all detectors individually, it is strongly pronounced and in this case the shadow showed a gradient over the full N-signal range. Moreover the signal can be at least roughly simulated with the developed program, to learn more about the sample structure. For further validation better defined reference samples are necessary.

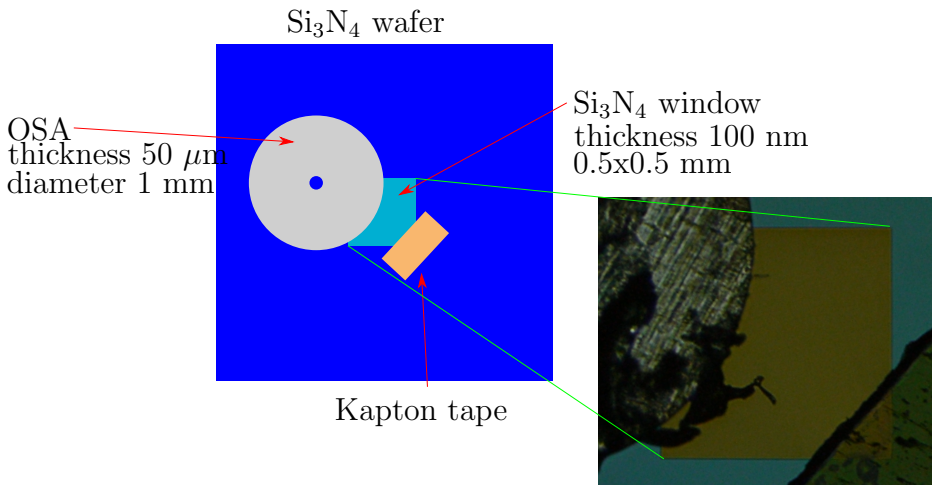


Figure 6.19: Illustration and visible light microscope image of the sample measured at BESSY II

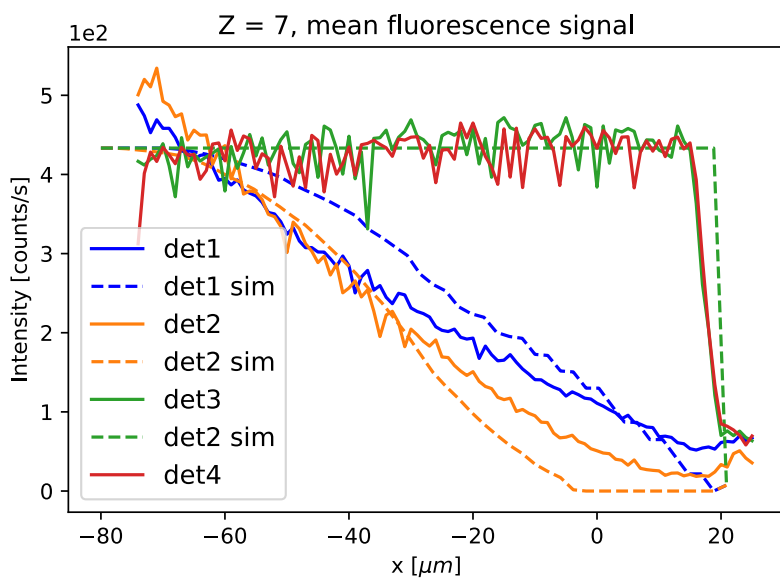


Figure 6.20: Nitrogen signal in the different detector elements, measured (solid lines) and simulated (dotted lines) for an excitation energy of 1.5 keV and a simulated intensity of 3.15×10^9 cps.

Chapter 7

Conclusion and Prospect

The ongoing technological development of X-ray fluorescence detectors with a large solid angle and new geometries has paved the way to fast imaging applications in the soft X-ray regime. A recent setup using a new annular QUAD detector, the AnImaX microscopy end station for soft X-ray imaging of bio-medical samples, was presented showing promising results considering resolution and measurement times. While improving the detected signal intensity, the large solid angle of the QUAD detector poses new challenges for the fluorescence data interpretation and quantification approaches, because the established theoretical description is only valid for the assumption of a small solid angle and narrow beams.

Especially for inhomogeneous samples the account of effects caused by a large solid angle of detection is a complex task which has not been tackled in a general way until now. Since the fluorescence radiation passes various parts of the inhomogeneous sample before being detected, the signal includes information about the absorption caused by surrounding sample domains, which is widely ignored in imaging data evaluation.

Modeling the experimental situation of the AnImaX end station, the simulation program QUADaps was developed based on traditional fundamental parameter calculations combined with a geometrical decomposition of sample and detector. The QUADaps program offers a flexible excitation source and sample design, mimics line and area scans common in microscopy applications and thus enables the pre-evaluation of the influence that the large solid angle of detection has on the signal.

First applications showed the applicability of QUADaps for various samples, ranging from homogeneous to structured to inhomogeneous samples with a light matrix and heavy inhomogeneities. The simulation predicted shadow-

ing and edge enhancement effects caused by the structures/inhomogeneities, which were confirmed by first experiments at the synchrotron. Thus the study of these kind of absorption effects is shown to be of considerable importance for the correct interpretation of imaging data aimed at quantitative evaluation.

Furthermore the additional information due to the 4-cell geometry of the QUAD detector was shown to make the effects more prominently visible. It yet has to be evaluated whether the additional information outweigh the prolonged measurement times. In addition to better understanding the previously mentioned effects, it is likely that new effects, such as those caused by complex asymmetrical structures, could only be identified properly with independent measurements.

Additional experiments are necessary in order to learn more about the influence certain inhomogeneities have on the actual measurements and further validate the program. For a systematical study, QUADaps can be used to plan reference samples for certain applications.

Therefore, as a next step, the simulation of well-defined samples to determine lower limits of detection for the shadow effects is suggested, e.g. in form of cross-sections of a multilayered sample composed of light matrices with varying percentages of metal atoms. Validating the simulations with measurements of these samples would be the first step on a path to include such effects in the data evaluation necessary for quantitative imaging.

If the validation shows good agreement, QUADaps can be used as a tool to estimate various absorption effects for a wide range of sample classes. Based on these studies new semi-quantification evaluation procedures for different sample types can be established, leading to a better understanding of imaging data.

Acknowledgements

This thesis would not have been possible without the great support of my colleagues, family and friends. I want to thank all of you who have accompanied me through the last months and made this work a great experience. My special thanks goes to my supervisors: Birgit, Lars and Burkhard - thank you so much for the constant inspiration and guidance, I learned a lot and am still eager to learn more.

The experiments connected with my simulations would have been impossible without the AnImaX team (Konstantin, Andreas, Aurélie, Conrad and Felix) and the kind support of the PTB Berlin. The beamtimes with you were always fun and a very welcome change to my ‘dry’ programming.

Altogether my time in the AG Kanngießer at TU Berlin will always stay in good memory and I want to thank the whole group for your friendship and the great working atmosphere.

Besides the academic support I am very thankful for the open ears, helpful suggestions and general friendship of my family and friends: your willingness to proof-read, motivate and support me in so many other ways, helped me a lot! In particular I want to mention Jan, Jakob, Anne, Leon, Rike, Thea and Mhairi - thanks!

Last but not least I want to thank my family: Bärbel, Jörn, Ludwig and my grandmothers. The constant feeling of security your unconditional love always provided, is the biggest gift anyone could ask for.

Bibliography

- [1] E. Abbe. Beiträge zur Theorie des Mikroskops and der mikroskopischen Wahrnehmung. *Arch. mikrosk. Anat. Entw. Mech.*, 9:413, 1873.
- [2] K. Andrianov, L. Lühl, T. Nisius, A. Haidl, R. Gnewkow, L. Lötgering, H. Dierks, B. Kanngießer, and T. Wilhein. Scanning Transmission X-ray Microscopy with X-ray Fluorescence Detection at the XUV Beamline P04, PETRA III, DESY. *Journal of Physics: Conference Series*, 849(1):012007, 2017.
- [3] D. Attwood. *Soft X-Rays and Extreme Ultraviolet Radiation: Principles and Applications*. Cambridge University Press, 1999.
- [4] N. Langhoff R. Wedell H. Wolff (Eds.) B. Beckhoff, B. Kanngießer. *Handbook of Practical X-Ray Fluorescence Analysis*. Springer Verlag, 2006.
- [5] L. Bonizzoni, A. Maloni, and M. Milazzo. Evaluation of effects of irregular shape on quantitative xrf analysis of metal objects. *X-Ray Spectrometry*, 35(6):390–399, 2006.
- [6] Bruker. QUANTAX FlatQUAD, 2014. DOC-B82-EXS012, Rev. 1.0 [Online; accessed March 27, 2018].
- [7] W.Z. Chang and D.B. Wittry. Calculation of x-ray fluorescence intensities for convergent x-ray beams. *Microbeam Analysis*, 3:23–32, 1994.
- [8] D. K. de Boer. Angular dependence of x-ray fluorescence intensities. *X-ray Spectrometry*, 18:119–129, 1989.
- [9] D. K. de Boer. Calculation of x-ray fluorescence intensities from bulk and multilayer samples. *X-ray Spectrometry*, 19:145–154, 1989.
- [10] J. Bufon et.al. Towards a multi-element silicon drift detector system for fluorescence spectroscopy in the soft x-ray regime. *X-Ray Spectrometry*, 46(5):313–318, 2017. XRS-16-0088.R1.

- [11] Oxford Instruments. Silicon drift detectors explained. [Online; accessed March 21, 2018].
- [12] International Tables for Crystallography. X-ray crossections carbon, Vol. C. [Online; accessed February 08, 2018].
- [13] W. Malzer. Calculation of attenuation and x-ray fluorescence intensities for non-parallel x-ray beams. *X-ray Spectrometry - X-RAY SPEC-TROM*, 32:106–112, 03 2003.
- [14] M. Mantler and N. Kawahara. How accurate are modern fundamental parameter methods? *The Rigaku Journal*, 21(2):17–25, 2004.
- [15] G.V. Pavlinsky and B.I. Kitov. Influence of divergence of the primary radiation beam on the line intensity of the x-ray fluorescence spectrum. *X-Ray Spectrometry*, 8(3):96–101, 1979.
- [16] J. Sherman. The theoretical derivation of fluorescent x-ray intensities from mixtures. *Spectrochimica Acta*, 7(Supplement C):283 – 306, 1955.
- [17] T. Shiraiwa and N. Fujino. Theoretical calculation of fluorescent x-ray intensities in fluorescent x-ray spectrochemical analysis. *Japanese Journal of Applied Physics*, 5:886, October 1966.
- [18] Wikipedia, the free encyclopedia, author Ulfund. X-ray ranges, 2012. [Online; accessed February 08, 2018].
- [19] N. J. Zaluzec. Analytical formulae for calculation of x-ray detector solid angles in the scanning and scanning/transmission analytical electron microscope. *Microscopy and Microanalysis*, 20(4):1318–1326, 2014.